Magnetometry: solving the fundamental ambiguity from line pair inversion

Véronique Bommier

LESIA, Observatoire de Paris, Université PSL, CNRS, Sorbonne Université, Université de Paris
5, Place Jules Janssen, 92190 Meudon, France

ABSTRACT

Context. All magnetic field vector measurements lead to ambiguous results.
Aims. We show that observations in two different lines belonging to the same multiplet but having different absorption coefficients so that they are formed at two different depths like Fe I 6302.5 Å and 6301.5 Å, enable the resolution of the azimuth ambiguity remaining from the Zeeman signal interpretation.
Methods. What is measured by interpretation of the Zeeman effect is the magnetic field H, and not the divergence-free magnetic induction B. We analyze how the anisotropy of the photosphere, which is strongly stratified due to gravity and density at the star surface, affects div H and how the ambiguity resolution has to be performed in these conditions.
Results. As a consequence, two ambiguity-resolved field vector maps are obtained at two different but close altitudes, which enable the derivation of the current density full vector via rot $H = J$. This reveals the horizontal component of the current density, which is generally found markedly larger than the better known vertical one. We observe some systematical trends, of which we present examples in the paper, like circular currents wrapping spots clockwise about a positive polarity spot and anticlockwise about a negative polarity spot and strong horizontal current components crossing active region neutral lines.
Conclusions. We finally remark that the Na I D1 and D2 lines form another such line pair and we successfully tested their application to full vector mapping (magnetic field and current density) with THÉMIS telescope observations. Therefore, we propose them as an access to the low chromosphere where they are formed. Examples of such observations are also reported in the paper.

Key words. Magnetic fields – Polarization – Sun: magnetic fields – Sun: photosphere – Sun: chromosphere – Sun: magnetic topology

1. Introduction

In solar atmosphere, magnetic field and electric currents are strongly coupled via the Ampère's circital law. Moreover, and without entering in details, the presence of strong electric currents, for instance under the form of a current sheet, could be the place where an eruptive event could occur. Thus, the knowledge of the electric current is essential for understanding the atmosphere stability and evolution for space weather purposes. However, the electric current vector components result from spatial derivatives of the magnetic field vector components via the Maxwell equation rot $H = J$. This makes them particularly difficult to derive from the observations because this requires a good accuracy for the primitive quantity (in the mathematical meaning), which is the magnetic field. This requires also that the magnetic field vector is fully known without any ambiguity. The Zeeman effect observation is ambiguous in terms of magnetic field vector because two field vectors symmetrical with respect to the line-of-sight, i.e., which have the same longitudinal component but opposite transverse components, are responsible for the same polarization. They are not discriminated at the spectropolarimetric data inversion step. This ambiguity is often referred to as the azimuth ambiguity, or 180° ambiguity, or fundamental ambiguity.

The derivation of the electric current full vector requires that the ambiguity is solved after the spectropolarimetric data inversion. A review of different methods can be found in Met-

calf et al. (2006). However, sunspots offer the opportunity of an intuitive solution of the ambiguity in their penumbra from the spot magnetic polarity. For a negative spot, the penumbra field vectors point towards the spot center, whereas for a positive spot the penumbra field vectors diverge from the spot center. Some authors took advantage of this opportunity to obtain current density vectors in spot penumbrae. Socas-Navarro (2005) applied the SIR code (Ruiz Cobo & del Toro Iniesta 1992) for the spectropolarimetric data inversion. This code uses several depth nodes, where the magnetic field is independently determined, which enables the derivation of the field variation along depth. The ambiguity intuitive solution was further introduced in the spot penumbra. Then, the full current density vector was derived in the spot. The same method was applied to HINODE/SOT/SP data by Puschmann et al. (2010). The quality of HINODE data permitted to show a coherence between the filamentary structure of the penumbra and the current density vector lines. Significant currents are seen to wrap around the hotter, more elevated regions with lower and more horizontal magnetic fields that harbor strong upflows and radial outflows (the intraspines).

Indeed, the derivation of the three coordinates of the current density vector requires the knowledge of the depth variations of the magnetic field, which is rarely achieved. In general, a single line is observed, which is formed at a given depth. Except when the SIR code or a code of similar technique is applied, the magnetic field is derived at this single depth and only the vertical component J_z of the current density can be finally derived. Thus, full vector current density determinations remain

rare. We present below such determinations, which are not based on the SIR code application, but on two line observations and single-line Milne-Eddington inversions. The inversion method is described in section 2. The depth difference in line formation altitude was previously directly derived from other HINODE/SOT/SP data (Faurobert et al. 2009). This enables the complete derivation of div H from the observations, which enables the ambiguity resolution, the method of which is described in section 3. In particular, we analyze how the anisotropy of the photosphere, which is strongly stratified due to gravity and density at the star surface, affects div H and how the ambiguity resolution has to be performed in these conditions. We present example results in section 4. As Puschmann et al. (2010), we obtain that the horizontal component of the current density vector is much stronger than the vertical one. The vertical component is the most frequently published and discussed. The horizontal component remained generally unknown, which is yet much larger. We discuss examples of typical structures we derived for the horizontal component, in sunspot penumbrae and across some neutral lines.

We tested our multiline ambiguity solution method on different spectral lines observed with the THÉMIS telescope operating in its new multislit mode. The two splitted beams enter the spectrograph by two parallel slits. As a consequence, the different spectral windows (Fe I 6301/6302, Na I D1, Na I D2) are not simultaneously observed but sequentially. As a result, we obtained that the pair of lines must belong to the same multiplet in order to be formed in the same manner, but with different absorption coefficients. This is the case of the Fe I 6301.5 Å and 6302.5 Å line pair. With these conditions, their depth formation difference remains rather constant as visible in the simulation by Khomenko & Collados (2007). This line pair is interestingly the one observed by HINODE/SOT/SP. We observed that the Na I D1 and D2 line pair obeys the same conditions. But their depth formation is higher in the solar atmosphere. It is located near the temperature minimum in the low chromosphere. Thus, they could provide the disambiguated magnetic field at this altitude. With the THÉMIS telescope, we observed also this line pair. After the magnetic inversion of the spectropolarimetric observations, we successfully resolved the ambiguity with this line pair. In sections 4.3 and 4.4, we present same regions observed with the Fe I 6301/6302 line pair (photospheric) and with the Na I D1/D2 line pair (chromospheric). We present the magnetic field maps observed in a sunspot penumbra and above a neutral line at the two altitude ranges, photosphere and low chromosphere respectively. In Sect. 5, we present a verification of our method, by applying available codes to the same solar data and by comparing the results.

It has to be recalled that what is measured by interpretation of the Zeeman effect is the magnetic field H, and not the magnetic induction B (Bommier 2020). The magnetic induction B is divergence-free, when the magnetic field H is not. They are related by $B = \mu_0(H + M)$, where M is the magnetization. However, in usual solar models, the reported electron density is such that the modulus of M is very small, with respect to the modulus of H, which results in $B \approx \mu_0 H$, which makes H quite divergence-free also. In this respect, minimizing div H makes sense for solving the ambiguity. However, the Sun's surface electron density could be much higher due to electron thermal escape in the solar interior, where the electron thermal velocity overpasses the star gravitation escape velocity by a factor of 14 and the proton escape velocity by a factor of 6, as remarked by Bommier (2020). The model electron density is in

fact derived from ionization equilibria modelled from the spectrum, and in addition within the local electric neutrality hypothesis (Vernazza et al. 1973, Section V), which has to be questioned in the presence of the star gravitation field as explained above. Thus, div H could be non-zero as observed (see the review by Balthasar 2018), but its minimization could be kept as a method for solving the fundamental ambiguity. The results presented in the present paper confirm this approach.

In practice, we will apply Gauss units for describing the magnetic field. They are in fact units for $\mu_0 H$.

2. Data Analysis First Step: Milne-Eddington Inversion

We applied the Milne-Eddington inversion code UNNOFIT. Based on the Unno-Rachkovsky solution of the transfer equation for the radiation Stokes parameters of a spectral line, the code accounts for all the magneto-optical effects (Landolfi & Landi Degl'Innocenti 1982). The code applies the Levenberg-Marquardt algorithm to the theoretical profile to make it fitting the observed profile. Eight parameters were entered in the algorithm, which are namely: the line center frequency λ_0, the Doppler width $\Delta\lambda_D$, η_0, the three magnetic field coordinates, the Voigt parameter a, and the ratio B_1/B_0 of the two parameters characterizing the Milne-Eddington atmosphere. This was the original code developed by Landolfi et al. (1984).

However, since the pioneering work by Stenflo (1973), it is well known that the atmosphere is permeated by unresolved magnetic structures, which can be roughly modelled with a magnetic filling factor α. Stenflo's analysis is based on magnetic field measurements from the two Fe I 5247.1 Å and 5250.2 Å lines, which are two lines of the same multiplet but with identical absorption coefficients, so that they are formed at the same depth. They have different Landé factors and then different magnetic sensitivities. This enabled the unresolved magnetic structures discovery. We introduced the magnetic filling factor α as the ninth parameter of the UNNOFIT inversion, in the Levenberg-Marquardt algorithm. In other words, denoting by 'm' and 'nm' the magnetic and non-magnetic contributions, one has for the four Stokes profiles, to which the algorithm is applied

$$\begin{cases} I = (1 - \alpha)I_{nm} + \alpha I_m \\ Q = \alpha Q_m \\ U = \alpha U_m \\ V = \alpha V_m \end{cases}. \tag{1}$$

The magnetic and non-magnetic contributions are computed from the Unno-Rachkovsky solution with all their physical parameters taken as equal except for the presence or absence of the three magnetic field coordinates. In other words, the dependencies are $I_m(\lambda_0, \Delta\lambda_D, \eta_0, H, \theta_H, \varphi_H, a, B_1/B_0)$ and $I_{nm}(\lambda_0, \Delta\lambda_D, \eta_0, a, B_1/B_0)$, where (H, θ_H, φ_H) are the three spherical coordinates of the magnetic field vector: strength, inclination, and azimuth. In the present work, the same weight of unity was given to the four Stokes parameters for the chi-square calculation because I plays an important role for the determination of α (usually, I is less weighted).

We tested the code and validated it (Bommier et al. 2007), but we obtained that the unresolved magnetic field strength H and the magnetic filling factor α cannot be separately determined (see Fig. 4 of that paper). H is here the modulus of the magnetic field vector, which is different from its longitudinal component. Only their product αH, which is the local average magnetic field strength, is obtained as final result. This occurs when the field is

not strong enough to well separate the Zeeman components with respect to the Doppler width (typically 1000 G at least). This is the effect of the larger number of parameters to be determined with respect to the number of independent parameters provided by the line observation. A line is characterized by a position, a width, a central depth, and three Stokes parameters, which enable the calculation of the three magnetic field components. This results in only 6 independent parameters. The Voigt a parameters characterizes the far wings and plays a specific role there. Thus, with the filling factor, the number of searched for parameters exceeds the number of available parameters. However, as shown by the tests, the local average magnetic field stregth αH is finally well determined. Later on, a tenth parameter was introduced in the inversion, which is the velocity gradient along the line formation depth, which depends on an additional observed parameter, which is the line asymmetry (Molodij et al. 2011).

The validation was achieved by creating test profiles from the Unno-Rachkovsky solution, which we submitted to the inversion code. We thus compared the ouput magnetic field values with the input ones. We analyzed 183,600 theoretical profiles. The details of their definition are given in Bommier et al. (2007), Sect. 2.2. The theoretical initial profiles were noised at the 1.5×10^{-3} level for the polarimetric noise, which is not far from the HINODE/SOT/SP one that we evaluated at 1.2×10^{-3} in profile far wings (1.0×10^{-3} during our last THÉMIS campaigns described in this paper). This informed us also about the accuracy of the inversion method by looking at the widths of the histograms of the difference between input and output, which we plotted in Fig. 5 of Bommier et al. (2007). We thus obtained accuracies of 15 G on the field strength (averaged with the magnetic filling factor, αH), 5° on the field inclination and azimuth for $\alpha \mu_0 H > 45$ G, and 20 G on the field strength, 10° on the field inclination, and 15° on the field azimuth for $\alpha \mu_0 H < 45$ G, for the 1.5×10^{-3} level of polarimetric noise, for Fe I 6302.5 Å. For 6301.5, the values are similar for $\alpha \mu_0 H > 45$ G and a bit larger for $\alpha \mu_0 H < 45$ G, due to the lower magnetic sensitivity, which results from the lower effective Landé factor of this line (see Fig. 7 of the same paper).

The inversion is performed in the four Stokes profiles simultaneously. It is well-known that in weak fields the linear polarization Stokes parameters (Q, U) depend quadratically on the transverse magnetic field, whereas the circular polarization Stokes parameter V depends linearly on the longitudinal magnetic field. As the chi-square of the four Stokes parameter are simply added in the algorithm, the longitudinal and transverse fields are simultaneously determined in a unique procedure. This results in quite comparable accuracies. We plotted the difference histograms for the cartesian components $\mu_0 H_x, \mu_0 H_y, \mu_0 H_z$ in the line-of-sight reference frame assumed to be at disk-center for the same test data as above. We obtained quite comparable widths or inaccuracy of 15 G for $\mu_0 H_x$ and $\mu_0 H_y$, and 10 G for $\mu_0 H_z$, for $\alpha \mu_0 H > 10$ G.

Although the inversion finally provides only the $\alpha \mu_0 H$ product, it is important to take α into account during the inversion for a good determination of the field inclination (Leka et al. 2022). Due to the sensitivity difference between the longitudinal and transverse fields, forcing $\alpha = 1$ (i.e., ignoring α) would lead to bad inclinations in regions where α is far from unity.

Landolfi et al. (1984) developed the light UNNOFIT version for the normal Zeeman triplet, and the heavier UNNOFIT2 version specific for Zeeman multiplets. More details are given in Bommier (2013). We were thus able to treat any kind of line.

3. Data Analysis Second Step: Azimuth Ambiguity Resolution

We applied a modification to the ME0 code developed by Metcalf, Crouch, Barnes, & Leka and now available on the web[1] (Leka et al. 2009). This code applies the "Minimum Energy" Method initially described by Metcalf (1994), which consists in searching for the field vector orientation that minimizes $|div \, \boldsymbol{H}| + \lambda |J_Z|$, where $\boldsymbol{J}$ is the current density vector, J_Z its vertical component, and λ a positive weight parameter usually fixed at unity (with $\boldsymbol{H}$ expressed in Gauss). Minimizing $|div \, \boldsymbol{B}|$ is a natural requirement imposed by Maxwell's equations. As explained in the Introduction, we will extent this requirement to what is really measured, i.e., $|div \, \boldsymbol{H}|$. On the other hand, minimizing the current density minimizes the maximum allowed free magnetic energy (Metcalf 1994). The minimization is performed globally on the whole map by applying the "simulated annealing" algorithm. Its application to this minimization problem is described by Crouch et al. (2009). The method is then complemented by propagating the solution via the acute angle method below a certain field strength threshold (Leka et al. 2009) presently taken at 400 G. The acute angle method consists in selecting from two ambiguous solutions symmetrical with respect to the line-of-sight, the solution that makes an acute angle (in the transverse plane) with the vector to be compared. In the original ME0 method, one single map is used and the vertical derivatives of the magnetic field are derived from a current-free reconstruction of the magnetic field. Reconstructions based on less restrictive hypotheses were later on introduced by this method authors (Metcalf et al. 2006; Leka et al. 2009). As the field vector ambiguity concerns its transverse component in the line-of-sight coordinates, whereas the reconstruction is performed in the heliographic coordinates, back and forth transformations have to be performed between these two systems of coordinates.

More precisely, $div \, \boldsymbol{H}$ is calculated in the heliographic reference frame in the original ME0 code because $\partial H_z / \partial z$ is evaluated in this frame by the reconstruction. Our approach avoids the vertical reconstruction of the field by the introduction of two maps recorded in two lines formed at two different depths. In our method we kept the minimization procedure of ME0 but we calculated $div \, \boldsymbol{H}$ in the line-of-sight coordinates instead, which was possible from our 2-line observations. We accordingly modified the corresponding subroutine of ME0. We calculated the expression of $div \, \boldsymbol{H}$ adapted to the case of a line formation plane inclined with respect to the line-of-sight in order to develop a method able to treat maps of any location on the solar disk. Below and in Appendix A, we describe this calculation. A different calculation, which also accounts for the case of a line-of-sight inclined with respect to the local vertical, was developed by Crouch et al. (2009); Crouch (2013, 2015). We have first to introduce the various reference frames entering the calculation.

3.1. Reference frames

Our approach is in agreement with Gary & Hagyard (1990) in the limit $P = 0$. In the following, we denote as $Oxyz$ the line-of-sight (l.o.s.) reference frame and $OXYZ$ the heliographic one at the observed region location. The l.o.s. reference frame is defined by Oz being the l.o.s. itself oriented towards the observer, and Oy being parallel to the disk central meridian oriented towards the solar north. The heliographic reference frame has OX aligned with the local parallel solar west oriented, OY aligned

with the local meridian solar north oriented, and OZ along the solar radius oriented from the Sun's center towards outside. We denote as $\boldsymbol{R}$ the unit vector along the OZ axis of the heliographic reference frame, which is also the local solar radius. We denote with indexes (x, y, z) the vector coordinates in the l.o.s. reference frame, and (X, Y, Z) those in the heliographic reference frame. Gary & Hagyard (1990) denote with the upper index l the vector coordinates in the l.o.s. reference frame, and h those in the heliographic reference frame. In the l.o.s. reference frame, the $\boldsymbol{R}$ coordinates are

$$\begin{cases} R_x = \sin(L - L_c) \cos b \\ R_y = \sin b \cos b_0 - \cos(L - L_c) \cos b \sin b_0 \\ R_z = \sin b \sin b_0 + \cos(L - L_c) \cos b \cos b_0 \end{cases}, \qquad (2)$$

where L and b are, respectively, the longitude and latitude of the center O of the observed region, L_c is the disk central meridian longitude, and b_0 is the disk center latitude. The other unit vectors of the $OXYZ$ heliographic reference frame are denoted as $\boldsymbol{I}$ along OX and $\boldsymbol{K}$ along OY, with

$$\begin{cases} I_x = \cos(L - L_c) \\ I_y = \sin(L - L_c) \sin b_0 \\ I_z = -\sin(L - L_c) \cos b_0 \end{cases} \qquad (3)$$

and

$$\begin{cases} K_x = -\sin(L - L_c) \sin b \\ K_y = \cos b \cos b_0 + \cos(L - L_c) \sin b \sin b_0 \\ K_z = \cos b \sin b_0 - \cos(L - L_c) \sin b \cos b_0 \end{cases} \qquad (4)$$

in the l.o.s. reference frame. These formulae are obtained by applying 3 rotations successively to transform the heliographic reference frame into the l.o.s. one, namely: 1/ rotation of b about the OX axis; 2/ rotation of $-(L - L_c)$ about the new OY axis; 3/ rotation of $-b_0$ about the new Ox axis. Conversely, the coordinates of the l.o.s. basic unit vectors $\boldsymbol{i}$, $\boldsymbol{k}$ and $\boldsymbol{\ell}$ (l.o.s. vector) in the heliographic reference frame are

$$\begin{cases} i_X = \cos(L - L_c) \\ i_Y = -\sin(L - L_c) \sin b \\ i_Z = \sin(L - L_c) \cos b \end{cases} \qquad (5)$$

and

$$\begin{cases} k_X = \sin(L - L_c) \sin b_0 \\ k_Y = \cos b \cos b_0 + \cos(L - L_c) \sin b \sin b_0 \\ k_Z = \sin b \cos b_0 - \cos(L - L_c) \cos b \sin b_0 \end{cases} \qquad (6)$$

and

$$\begin{cases} \ell_X = -\sin(L - L_c) \cos b_0 \\ \ell_Y = \cos b \sin b_0 - \cos(L - L_c) \sin b \cos b_0 \\ \ell_Z = \sin b \sin b_0 + \cos(L - L_c) \cos b \cos b_0 \end{cases}. \qquad (7)$$

The transformation from the coordinates (x, y, z) of a given vector in the l.o.s. reference frame into its coordinates (X, Y, Z) in the heliographic reference frame, can be written as

$$\begin{cases} X = x i_X + y k_X + z \ell_X \\ Y = x i_Y + y k_Y + z \ell_Y \\ Z = x i_Z + y k_Z + z \ell_Z \end{cases} \qquad (8)$$

and conversely

$$\begin{cases} x = X I_x + Y K_x + Z R_x \\ y = X I_y + Y K_y + Z R_y \\ z = X I_z + Y K_z + Z R_z \end{cases}. \qquad (9)$$
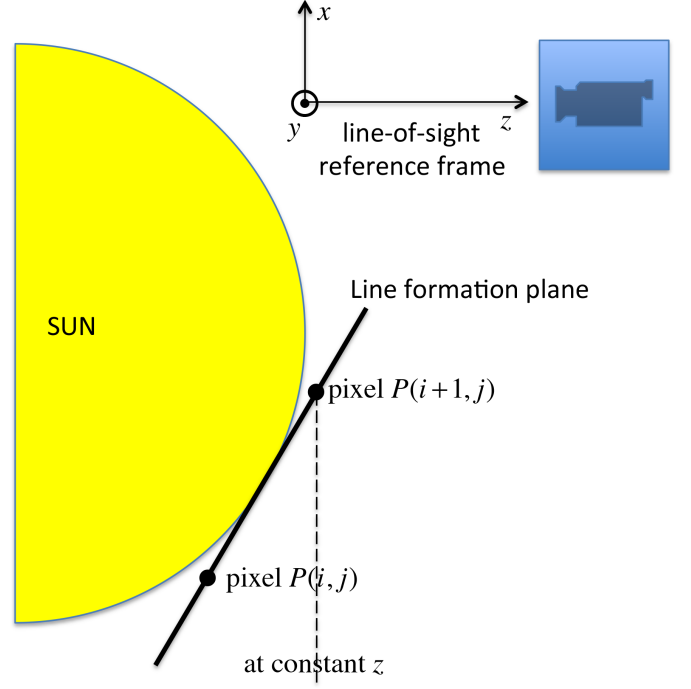
Fig. 1. $\Delta_x H_x^{(m)}$ is the difference between the H_x components measured in pixels $P(i + 1, j)$ and $P(i, j)$. It can be seen that the z coordinate is not the same for the two pixels for an observation out of disk center, which is in contradiction with the definition of the partial derivative along x.

3.2. Deprojection

A map is obtained from a scan of the spectrograph slit along the solar image. The map is reconstructed by positioning side by side all the slit outputs. The mapped quantities are then given on a rectangular system of pixels in the l.o.s. reference frame, the Δx pixel size along Ox being given by the scan step size and the Δy pixel size along Oy being given by the camera pixel size. Thus $\Delta x \neq \Delta y$ in general, which results in an anamorphosis of the map. Once the ambiguity is solved and a single magnetic field vector is obtained for each pixel, its coordinates may be transformed into the heliographic reference frame. The deprojection of the pixel array is a more complicated task because the meshs are no more rectangular in general, as described for instance in Gary & Hagyard (1990). In the present paper and related studies, we have roughly approximated a rectangular shape for the deprojected map, however, with pixel side sizes of $\Delta X = \Delta x / I_x$ and $\Delta Y = \Delta y / K_y$. This is exact when the map center is located on the solar equator and when $b_0 = 0$. This departs from exactitude when the latitudes of the disk and/or map centers depart from 0. The cosine of the heliocentric angle θ is $\mu = R_z$.

3.3. The quantity to be minimized

As stated above, we applied the "simulated annealing" algorithm to globally minimize $|\text{div } \boldsymbol{H}| + \lambda |J_Z|$. The parameter λ was taken as unity (with $\boldsymbol{H}$ expressed in Gauss). Indeed, in his pioneering paper, Metcalf (1994) recommends to minimize the alternative quantity $|\text{div } \boldsymbol{H}| + \lambda \|\boldsymbol{J}\|$ as the physically meaningful quantity for "energy minimization", with the full current vector and not only its Z-component. We first tried this minimization because we had also the transverse current component (within the ambiguity) from our 2-line observations, but it did not converge correctly. On the contrary, we found that the algorithm sucess-

fully worked out, when we instead minimized $|\text{div } \boldsymbol{H}| + \lambda |J_Z|$ with $\lambda = 1$. We tried various λ values and also found $\lambda = 1$ to be the best choice, which leads to maps at most free of articifial defaults like strong current lines delineating zones of different ambiguous solution choice by the algorithm, or with minimal checkered zones where the ambiguity resolution failed. The minimization of $|\text{div } \boldsymbol{H}| + \lambda |J_Z|$ was later performed also by Metcalf's team (Metcalf et al. 2006).

However, the map under study is usually not located at disk center, which results in a certain inclination of the map formation plane with respect to the l.o.s. referred to by the heliocentric angle θ and its cosine $\mu = \cos \theta$. We denote as "map formation plane" the heliographic horizontal plane, i.e., the plane perpendicular to the local solar radius. The map results from interpretation of polarization in spectral lines. As explained below in Sect. 3.4, the radiation received along the line-of-sight in a given spectral line comes essentially from a certain height in the solar atmosphere (this is the Eddington-Barbier approximation), which defines an heliographic horizontal plane, which contains the location of the points where the magnetic field is measured by spectropolarimetry. This plane is not perpendicular to the line-of-sight, when the observed region is not located at disk center.

But the divergence has to be computed in a rectangular reference frame. For doing this, there are two possibilities. Either the coordinates of the two ambiguous magnetic field vectors obtained in the line-of-sight reference frame and symmetrical with respect to the line-of-sight, which are of the $H^{(l)}$ type, are transformed into heliographic coordinates of the $H^{(h)}$ type of Gary & Hagyard (1990). The ambiguity is then resolved in the heliographic reference frame, where the measurements are all located in the horizontal plane perpendicular to the OZ axis. This is the method applied by Leka et al. (2009) in their ME0 code described above. Or, as for us, we resolved the ambiguity in the line-of-sight coordinates of the field as obtained from the measurements, which are of the $H^{(l)}$ type of Gary & Hagyard (1990). In this case, the measurements are located along a plane inclined with respect to the line-of-sight, which is the Oz axis. This inclination described below and in Fig. 1 is at the origin of balancing terms in the divergence and curl expressions in terms of line-of-sight or $H^{(l)}$-type magnetic field vector coordinates, as derived in Appendix A.

In Appendix A we derive the expressions of $\text{div } \boldsymbol{H}$, J_Z and $J_{x,y}$ as a function of the l.o.s. reference frame magnetic field coordinates, when the fields are measured along an inclined formation plane perpendicular to the local solar radius unit vector $\boldsymbol{R}$ of l.o.s. components $R_{x,y,z}$ given in Eq. (2). We obtain

$$\text{div } \boldsymbol{H} = \frac{\Delta_x H_x^{(m)}}{\Delta x} + \frac{\Delta_y H_y^{(m)}}{\Delta y} + \frac{\Delta_z H_z^{(m)}}{\Delta z} \tag{10}$$
$$+ \frac{R_x}{R_z}\frac{\Delta_z H_x^{(m)}}{\Delta z} + \frac{R_y}{R_z}\frac{\Delta_z H_y^{(m)}}{\Delta z} \ .$$

We denote as $\boldsymbol{H}^{(m)}$ the vector measured along the inclined plane, where the line is formed. $Oxyz$ is the l.o.s. reference frame and Oy is solar north oriented. $\Delta_x H_x^{(m)}$ and $\Delta_y H_y^{(m)}$ are respectively the difference of the measured component $H_x^{(m)}$ or $H_y^{(m)}$ between two neighboring pixels in x or y direction. Δx or Δy denotes the distance between the neighboring pixels in the "sky plane", which is the plane perpendicular to the l.o.s. at the location of the observed region. The magnetic field may eventually be averaged between the two lines. If this average has to be performed before the ambiguity is solved, the acute angle method is applied

between the two lines to select the ambiguous solutions to average. This is a reasonable approximation, which saves computation time in the simulated annealing. This corresponds to assume that the field lines do not twist so much. As for $\Delta_z H_z^{(m)}$, it is the difference between the values obtained from the two lines with a difference in depth formation Δz along the l.o.s.. Explicit definitions of all these quantities are given in Appendix A. The way of calculating these quantities is detailed at the beginning of the Appendix. When the map center is located on the solar equator and when $b_0 = 0$, the above Eq. (10) simplifies in

$$\text{div } \boldsymbol{H} = \frac{\Delta_x H_x^{(m)}}{\Delta x} + \frac{\Delta_y H_y^{(m)}}{\Delta y} + \frac{\Delta_z H_z^{(m)}}{\Delta z} \tag{11}$$
$$+ \tan \theta \frac{\Delta_z H_x^{(m)}}{\Delta z}$$

where θ is the heliocentric angle (positive for the West side of the central meridian and negative for the East side). The second line of these equations accounts for the z variation hidden in $\Delta_x H_x^{(m)}/\Delta x$ and $\Delta_y H_y^{(m)}/\Delta y$, because $H^{(m)}$ is measured along the line formation plane which is not perpendicular to Oz in the general case.

In other words, if one considers two neighboring pixels, referred to as $P(i, j)$ and $P(i + 1, j)$, separated by the length Δx in the plane perpendicular to the line-of-sight, and if one considers a quantity A measured via the same line at the two places, namely $A_{i,j}$ and $A_{i+1,j}$, the ratio $(A_{i+1,j} - A_{i,j})/\Delta x = \Delta_x A/\Delta x$ is not an approximate value of the partial derivative $\partial A/\partial x$ because $\Delta_x A$ also involves a variation along the line-of-sight z together with the variation in x, when the observation is not performed at disk center, i.e., when the line formation plane is not perpendicular to the line-of-sight. From the definition, $\partial A/\partial x$ has to be evaluated at constant y and z. In the evaluation of $\Delta_x A = A_{i+1,j} - A_{i,j}$, one has $z[P(i + 1, j)] \neq z[P(i, j)]$, as it is visible in Fig. 1, when the line formation plane is inclined with respect to the line-of-sight, which is also the Oz axis. As a consequence, z is not kept constant in the partial derivative numerical evaluation, when the observation is done out of disk center. This was the reason to perform the Appendix A calculations. This problem was addressed in a different way by Crouch et al. (2009); Crouch (2013, 2015). However, the final results are in agreement, when observation data are treated as described below in Sect. 5.

For numerical computation, the divergence was computed at the center of a pixel, by averaging between the variations along each side of the pixel. We use two lines formed at two different depths. This results in

$$\Delta_x H_x^{(m)} = (H_x^{(1)}(i + 1, j) - H_x^{(1)}(i, j) \tag{12}$$
$$+ H_x^{(1)}(i + 1, j + 1) - H_x^{(1)}(i, j + 1)$$
$$+ H_x^{(2)}(i + 1, j) - H_x^{(2)}(i, j)$$
$$+ H_x^{(2)}(i + 1, j + 1) - H_x^{(2)}(i, j + 1))/4 \ ,$$

$$\Delta_y H_y^{(m)} = (H_y^{(1)}(i, j + 1) - H_y^{(1)}(i, j) \tag{13}$$
$$+ H_y^{(1)}(i + 1, j + 1) - H_y^{(1)}(i + 1, j)$$
$$+ H_y^{(2)}(i, j + 1) - H_y^{(2)}(i, j)$$
$$+ H_y^{(2)}(i + 1, j + 1) - H_y^{(2)}(i + 1, j))/4 \ ,$$

$$\Delta_z H_z^{(m)} = (H_z^{(2)}(i, j) - H_z^{(1)}(i, j) \tag{14}$$
$$+ H_z^{(2)}(i + 1, j) - H_z^{(1)}(i + 1, j)$$
$$+ H_z^{(2)}(i, j + 1) - H_z^{(1)}(i, j + 1)$$
$$+ H_z^{(2)}(i + 1, j + 1) - H_z^{(1)}(i + 1, j + 1))/4 \ ,$$

where the indexes (1) and (2) correspond to "line 1" and "line 2".

For the current density vector component J_Z along the direction perpendicular to the inclined plane we obtain (curl of the magnetic field)

$$J_Z = R_z \left[\frac{\Delta_x H_y^{(m)}}{\Delta x} - \frac{\Delta_y H_x^{(m)}}{\Delta y} \right] \tag{15}$$
$$+ R_x \frac{\Delta_y H_z^{(m)}}{\Delta y} - R_y \frac{\Delta_x H_z^{(m)}}{\Delta x} \ .$$

It is possible to obtain analogously the two components of the current density vector in the plane perpendicular to the line-of-sight (see Appendix A)

$$J_x = \left[\frac{\Delta_y H_z^{(m)}}{\Delta y} - \frac{\Delta_z H_y^{(m)}}{\Delta z} \right] + \frac{R_y}{R_z} \frac{\Delta_z H_z^{(m)}}{\Delta z} \ , \tag{16}$$

$$J_y = \left[\frac{\Delta_z H_x^{(m)}}{\Delta z} - \frac{\Delta_x H_z^{(m)}}{\Delta x} \right] - \frac{R_x}{R_z} \frac{\Delta_z H_z^{(m)}}{\Delta z} \ . \tag{17}$$

From these relations and by applying Eq. (8), the z component of the current density vector in the line-of-sight reference frame can be derived, which is

$$J_z = \left(J_Z - J_x R_x - J_y R_y \right) / R_z \ , \tag{18}$$

which can be reduced into

$$J_z = \left[\frac{\Delta_x H_y^{(m)}}{\Delta x} - \frac{\Delta_y H_x^{(m)}}{\Delta y} \right] \tag{19}$$
$$+ \frac{R_x}{R_z} \frac{\Delta_z H_y^{(m)}}{\Delta z} - \frac{R_y}{R_z} \frac{\Delta_z H_x^{(m)}}{\Delta z} \ .$$

The second line of the formula accounts for the inclination of the line formation plane with respect to the line-of-sight. J_X and J_Y can then be derived by applying Eq. (8) to J_x, J_y and J_z.

In the following, we have plotted the heliographic reference frame components $J_{X,Y,Z}$ of the current density vector. For our plots, we derived the current density vector coordinates in the heliographic reference frame from the magnetic field unique vector (after disambiguation) rotated into the heliographic reference frame by applying Eq. (8).

Crouch et al. (2009); Crouch (2013, 2015) developed a different calculation for also accounting for the departure from disk center, which implies that the line-of-sight is not perpendicular to the line formation plane. They also obtained that additional terms have to be introduced into the usual divergence expression. But their formula given in Eqs. (4-5) of Crouch et al. (2009); Crouch (2013, 2015) is different from our Eq. (10) because the corresponding reference frames are not the same. The divergence of Crouch et al. (2009); Crouch (2013, 2015) applies spatial derivatives with respect to the *heliographic X* and *Y* and *line-of-sight z* coordinates, which do not form a rectangular reference frame, whereas our divergence applies spatial derivatives with respect to all the line-of-sight (x, y, z) reference frame coordinates, including the fact that the observed lines are formed along inclined planes. A possible method of comparison is to run codes based on each formula on the same data. This is done in Sect. 5, where it can be seen that the results obtained by both methods are in excellent agreement in similar application conditions. Both approaches are different ways to treat the problem of the inclined line-of-sight.
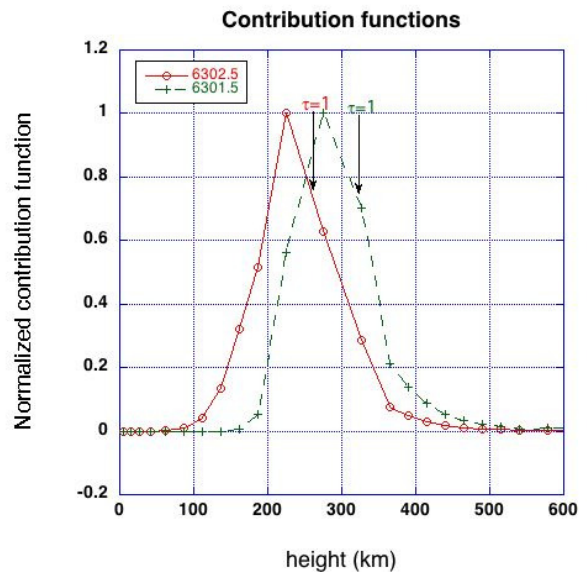
Fig. 2. Contribution functions of the two lines Fe I 6302.5 Å and 6301.5 Å as a function of the height above $\tau_{5000} = 1$. The heights where $\tau = 1$, which is the line formation height in the Eddington-Barbier approximation, are indicated by arrows.

3.4. The two line formation depth difference

The quantity to be determined is the difference in line-of-sight formation depth between the two lines. As it can be seen in Fig. 4 of Khomenko & Collados (2007), the two lines Fe I 6302.5 Å and 6301.5 Å are particularly interesting because their formation depths behave in a very parallel manner. As also visible in Fig. 4 of Khomenko & Collados (2007), such a parallelism is not the case for the pair of Fe I 6302.5 and 5250.2 lines. This was the reason why we discarded 5250.2, though it is more sensitive to the magnetic field than 6301.5. Such a parallelism probably originates in the fact that the two lines 6302.5 and 6301.5 belong to the same multiplet n. 816 and have different gf values, which are respectively $gf = 0.180$ for 6301.5 and $gf = 0.0627$ for 6302.5 from the Kurucz data-basis. Since differential non-LTE effects within multiplets are thought to be very small, as proven by detailed, multi-level, non-LTE computations, this implies that the absorption coefficient of 6301.5 is 3 times larger than the absorption coefficient of 6302.5. There is then no doubt that 6301.5 forms higher than 6302.5. In other words, the optical depth of 6301.5 is almost 3 where the optical depth of 6302.5 is unity. The Na I D1 and D2 lines form another such pair. They obey $gf = 1.309$ for Na I D2 and $gf = 0.655$ for Na I D1 (from the Kurucz data-basis), which are in a factor of 2 ratio. Thus Na I D2 forms higher than Na I D1.

The two iron line formation difference in the quiet sun atmosphere was recently determined by a phase-shift analysis of HINODE observations by Faurobert et al. (2009), who obtained the observed value 63.2 ± 0.9 km, which is corroborated by the value of 69 km derived by the same phase-shift technique applied to theoretical profiles computed with the non-LTE Uitenbroek's code (Grec et al. 2010).

However, it has to be remarked that the formation height varies along the line profile. The highest value, which is typically hundreds of km, is reached at line center, whereas in the far

wings, the formation height is nearly 0 km in the visible range. However, in the inversion algorithm, the mean squared difference between observed and theoretical profiles is computed over the whole profile. As the Zeeman effect is maximum around line center, this part of the profile is the most contributing to the field vector determination, so that it it is quite natural to assign the line center formation height to this field value. For instance, it is found that the value of $1/2 \arctan U/Q$ computed at line center provides the field azimuth within a very good first approximation.

In addition, it has to be remarked that the formation depth has a certain thickness, which is well represented by the behavior of the contribution function. We have plotted the contribution functions in Fig. 2 at line center for the two iron lines. This figure has been obtained by applying a non-LTE polarized radiation transfer code (Landi Degl'Innocenti et al. 1990; Bommier et al. 1991) to the Fe I 6302.5 and 6301.5 line formation in the quiet sun reference model atmosphere of Maltby et al. (1986) and in the absence of a magnetic field. It can be seen in the figure that the formation depth of each line has an accuracy of the order of ±75 km, which is the halfwidth of the contribution function. However, the difference $\Delta z = 66$ km between the two lines remains clearly visible all along the profile of the contribution function. In Fig. 2 we have also indicated with arrows the height of $\tau = 1$, which we consider as the line formation depth following the Eddington-Barbier approximation. It is well visible that this height correctly represents the mean line formation depth. Fig. 4 of Khomenko & Collados (2007) also shows that the formation depth difference remains on the order of $\Delta z = 70$ km in the quiet sun, whatever the formation depth is in itself.

Finally, in Fig. 4 of Khomenko & Collados (2007) we observed that the depth difference is larger in active regions than in quiet ones. We thus applied instead the depth difference of 98 km at disk center for active regions. This is also the value determined with the non-LTE Uitenbroek's code (Grec et al. 2010) in a previous approximation.

As for the Na I D lines, we derived their formation depths from a model that we describe below. The temperature, electron pressure, and gas pressure were first taken from an atmospheric model. We used the Maltby et al. (1986) quiet sun photospheric reference model extrapolated downwards beyond −70 km to −450 km below the $\tau_{5000} = 1$ level (courtesy of IAC). The continuum absorption coefficient was evaluated as in the MALIP code of Landi Degl'Innocenti (1976), i.e., by including H^- bound-free, H^- free-free, neutral hydrogen atom opacity, Rayleigh scattering on H atoms, and Thompson scattering on free electrons. The line absorption coefficient was derived from the Boltzmann and Saha equilibrium laws taking the two first ions of element into account. The atomic data were taken from Wiese or Moore and the partition functions from Wittmann. The iron abundance was assumed to be 7.60 and the sodium abundance 6.25 in the usual logarithmic scale where the abundance of hydrogen is 12. A depth-independent microturbulent velocity field of 1 km/s was introduced. Finally, departures from LTE in the ionization equilibrium were simulated for layers above $\tau_{5000} = 0.1$ by applying Saha's law with a constant radiation temperature of 5100 K instead of the electron temperature provided by the atmospheric model.

At final step, the line center optical depth grid was scaled to the continuum optical depth grid by applying the respective absorption coefficients. We used the continuum optical depth grid provided in the atmospheric model and the transfer equation was not explicitly solved again. The height of formation of the line center was then determined as follows. Once obtained the grid

of line center optical depths, the height of formation of the line center was located where the optical depth along the line of sight is unity (Eddington-Barbier approximation), i.e., where $\tau/\mu = 1$, where τ is the line center optical depth along the vertical and μ the cosine of the heliocentric angle θ (here supposed to be 0). As it can be seen in Fig. 5 of Bruls et al. (1991) and in Fig. 2 of the present paper, this conveniently represents the depth where the contribution function has its maximum.

We thus obtained quiet sun line center formation heights of 533 km for Na I D1 and 604 km for Na I D2 above the $\tau_{5000} = 1$ level, which are located in the low chromosphere close to the temperature minimum and with a difference of 71 km. We investigated also the Fe I 6302.5 and 6301.5 quiet sun line center formation heights. We obtained 262 km for 6302.5 and 328 km for 6301.5, leading to a difference of 66 km in excellent agreement with the measurements described above, which validates our computation method.

3.5. The aspect ratio of the strongly stratified atmosphere

We were indeed confronted with the problem that the vertical gradient of the magnetic field $\partial H_z/\partial z$ was found on the order of 3 G/km in spot umbrae, whereas the horizontal gradient $\partial H_x/\partial x + \partial H_y/\partial y$ was only on the order of 0.3 G/km. This leads to a non-vanishing value of div $\boldsymbol{H}$, whatever the signs would be. We then investigated the literature and found 15 references, which fully confirm these values provided by different instruments (groundbased as well as spaceborn), different inversion mesthods (SIR or others), and different spectral lines. The detailed description of these references can be found in Bommier (2013). An observation review was also presented by Balthasar (2018). All concluded to the above cited values. In other words, a loss of magnetic flux is observed with increasing height, which is not compensated for by an increase of the horizontal flux. In Bommier (2013) and Bommier (2014), we showed that the lack of spatial resolution in both transverse and along the line-of-sight directions cannot be held responsible for the seemingly non-vanishing observed div $\boldsymbol{H}$. This was based on mathematical study of the convolution procedure. It was shown that the divergence computed with averaged quantities is equal to the average of the local divergences. Accordingly, if the local divergence is zero, the divergence computed with averaged quantities should be also zero, within the noise level. The question arised to know if the observed value of div $\boldsymbol{H}$ is an effect of different spatial resolution along the different space directions. The effect of the spatial resolution, horizontal as well as vertical, is a filtering. The mathematical demonstration that the filtered divergence is the divergence of the filtered quantity is given in Bommier (2013) and Bommier (2014). Bommier (2014) includes also an easier demonstration in the spatial Fourier space. The same demonstration applies to the spatial averaging and the effect of the magnetic filling factor α. As explained in the previous section, we only know the "local average magnetic field " αH from the measurements, but the average divergence is the divergence of the averaged field. In addition, Bommier (2014) provides results of numerical tests devoted to investigate an eventual effect of the limited spatial resolution (eventually anisotropic). The numerical tests are all negative. They conclude to a zero divergence computed by finite differences, when the local divergence is zero. To our opinion, the negation of this logical proposition is that the non-zero observed value for the divergence indicates a non-zero local value. In Bommier (2015), we present a discussion about the necessity for div $\boldsymbol{H}$ to be zero. We argue that the existence of magnetic monopoles is not the only possibility

for a non-zero div $\boldsymbol{H}$. After a discussion about the measurement noise level effect, we present below another possibility we investigated.

In the THÉMIS measurements described in Bommier et al. (2007), which is the validation paper of the UNNOFIT inversion method, the polarimetric noise is assumed to be 1.5×10^{-3}. As reported in Sect. 2, this results in an inaccuracy of 10 G for the longitudinal field and 15 G for the transverse field. The field difference observed between and from the two line 6301.5 and 6302.5 is about 300 G, when the difference in line formation height is about 100 km, close to disk center. This results in an inaccuracy of 0.2 G/km for the vertical field gradient observed at disk center. As for the transverse field, the typical THÉMIS pixel size is about 500 km (Bommier 2013), which results in an inaccuracy of less than 0.2 G/km for the horizontal field gradient observed at disk center. The total inaccuracy on the observed div $\boldsymbol{H}$ value results in 0.4 G/km, to be compared to the non-vanishing value of 2.7 G/km, which results from the measurements reported in the literature. The non-vanishing value observed for div $\boldsymbol{H}$ is then markedly higher than the noise level.

We then investigated how the magnetic field is influenced by the plasma anisotropy due to the strong stratification due to the gravity and the density at the star surface, which is responsible for an "aspect ratio" between horizontal and vertical typical lengths. In the case of the solar photosphere, by applying strongly stratified fluid mechanics laws following Brethouwer et al. (2007), we evaluated this aspect ratio to be on the order of 20 (Bommier 2013, 2014) in the quiet sun photosphere. We proposed a physical process able to explain how the plasma strong stratification influences the magnetic field. The magnetic field is created by moving charges and we showed that the Debye screening applies also to moving charges. The anisotropy of the screening finally leads to possible non-vanishing of div $\boldsymbol{H}$. For a usual, spherical, Debye sphere, one has div $\boldsymbol{H} = 0$ (within negligible magnetization). The strong stratification is responsible for anistropy of the velocities, which results in a flattened Debye sphere and then to the possibility of div $\boldsymbol{H} \neq 0$. However, orders of magnitude concluded to a too weak resulting div $\boldsymbol{H}$ with respect to the observations. We then turned to the interior electron thermal escape (Bommier 2020) as the final explanation of the observations. Nevertheless, we finally showed in our observations that once the inverse of the aspect ratio is applied to scale the different magnetic field components, the scaled div $\boldsymbol{H}$ vanishes, which enables the ambiguity resolution. An example of this result in the case of NOAA 10808 observed with THÉMIS on 13 September 2005, is visible in Fig. 3 of Bommier (2013). Although we evaluated the theoretical value of the aspect ratio on the order of 20 in the quiet sun photosphere, this ratio may eventually be different in sunpots or plages or active regions, which is the case of the regions we treated. This is not so well-known and sometimes we adjusted the ratio (kept constant in the whole map) until the ambiguity resolution is consistent in the whole map. With the word "consistent" here, we mean that the resulting map does not show any artificial strong current line, which would delineate sharp azimuth change due to ambiguous solution selection change. The resulting map displays at most homogeneous field directions. We obtain that this inverse scaling is a necessity for a correct ambiguity resolution. The correctness is obtained by comparison with the intuitive ambiguity solution, which can be found in sunpot penumbrae as discussed in the following subsection. In Sect. 5.2 we obtain the same result by applying the inverse scaling before submitting the observation data to the available ambiguity resolution code AMBIG2.
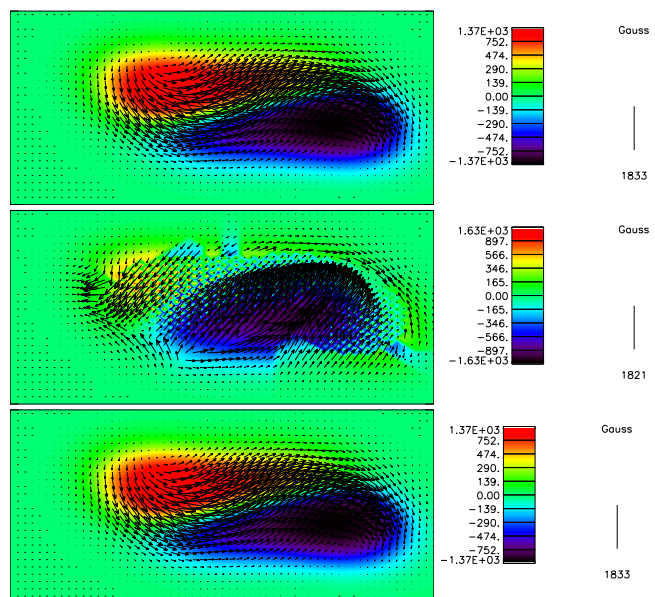
Fig. 3. Result of test of the ambiguity resolution by our method applied to theoretical data. Top: map of the input magnetic field vector. Middle: ambiguity resolution by applying the usual divergence formula (first line of Eq. (10) only) to these data, where the region is assumed to be out of disk center and where two lines formed at two different altitudes are supposed to be observed. Bottom: ambiguity resolution by applying Eq. (10).

It is also reported in Bommier (2015) that in the case of the photosphere flattened Debye sphere the current density remains given by curl $\boldsymbol{H} = \boldsymbol{J}$. We applied this law for the current density derivation from the magnetic field vector in different regions reported in the following.

3.6. Verification of the ambiguity resolution results

We thus treated 60 maps observed in Fe I 6301/6302 and 26 maps observed in Na I D with THÉMIS (in 2010-2013) and 23 HINODE/SOT/SP observations of active regions[2]. For the sunspots the correctness of the solution can be verified because the spot umbra polarity is known from circular polarization. This is true even near the limb, where the solar vertical field at spot center is nearly transverse with respect to the l.o.s.. The ambiguity solution is good if it is in agreement with the polarity. It has to be remarked that for a sunspot observed anywhere on the disk there is always a place in it where the ambiguity solution is can be derived from the spot polarity. This place is either in the penumbra, when the spot is observed near the disk center, or in the umbra, when the spot is observed near the limb. We consider such cases as possibilities of observational proofs of our disambiguation method, and we obtained successful proofs even in a spot at $\mu = 0.42$ which is $\theta = 65°$ from the disk center.

3.7. Test of the method on theoretical data

Our method for taking the departure from disk center into account, which leads to additional terms in the divergence formula Eq. (10), has been tested on theoretical data. Divergence-free data were prepared by simulating two close sunspots forming a δ-spot and by applying the magnetic field model described by Eqs. (8-10) of Fan & Gibson (2004). Simulation results based

---

[2] http://lesia.obspm.fr/perso/veronique-bommier/

pixel size	line	$\mathcal{M}_{\text{area}}$	$\mathcal{M}_{H_\perp > 100\,\text{G}}$	$\mathcal{M}_{H_\perp > 500\,\text{G}}$
0.3"	lower	0.99	1.00	1.00
0.3"	upper	0.99	1.00	1.00
0.9"	lower	0.99	1.00	1.00
0.9"	upper	0.99	1.00	1.00

Table 1. Performance metrics for the limited resolution case for our DIVB resolution algorithm applied to the test data of Leka et al. (2009) and Crouch (2013). The data were provided and the metrics were computed by K.D. Leka's courtesy.

noise level	$\mathcal{M}_{\text{area}}$	$\mathcal{M}_{H_\perp > 100\,\text{G}}$	$\mathcal{M}_{H_\perp > 500\,\text{G}}$
no	1.00	1.00	1.00
low	0.85	0.95	1.00
high	0.73	0.83	0.90

Table 2. Performance metrics for the noise-added case for our DIVB resolution algorithm applied to the test data provided by K.D. Leka's courtesy. These data were similar to that described in Crouch (2013), but with a two line formation height difference of 890 km along the l.o.s. instead. The metrics were computed by K.D. Leka's courtesy.

on this model have been used to study δ-spots (as in Fig. 3 of Leka et al. (2005)) and also to test various ambiguity resolution methods, as in Metcalf et al. (2006). The ambiguity of the transverse magnetic field in the line-of-sight reference frame was simulated and submitted to the ME0 ambiguity resolution code of Leka et al. (2009), which was modified by us for taking the vertical magnetic field gradient $\partial H_z / \partial z$ from 2-line observations instead from extrapolation as described at the beginning of Sect. 3. The 2-line observation had been simulated with theoretical results at two different depths separated by 70km along the line-of-sight. The pixel sizes are assumed to be $\Delta x = 1160$ km and $\Delta y = 581$ km as in our THÉMIS observations described in Bommier (2013). The δ-spot was assumed to be far from disk center and located at 30° from the central meridian in longitude and at 45° in latitude. The solar disk center latitude was assumed to be zero.

The test result is represented in Fig. 3, where the theoretical reference field is plotted in the top map. The result of the disambiguation when the usual divergence formula is applied, which is given by the first line of Eq. (10) only, is displayed in the middle map. The minimized quantity is in fact $|\text{div } \boldsymbol{H}| + \lambda |J_Z|$ with $\lambda = 1$ as in our method. It can be seen that the amiguity resolution widely fails over the δ-spot. When the full Eq. (10) is applied instead, the obtained result is displayed in the bottom map of Fig. 3, which is in total agreement with the reference field. It is thus confirmed by numerical test that the second line of Eq. (10) is necessary to resolve the ambiguity by applying a two-line analysis to maps observed out of disk center as discussed after Eq. (11) and in Fig. 1.

3.8. Test of the resolution code on theoretical data

We tested our ambiguity resolution code DIVB2 built on the above described method, on the theoretical test data described in Leka et al. (2009). These data were used for testing various ambiguity resolution methods as in Leka et al. (2009). The methods by Crouch et al. (2009); Crouch (2013, 2015), where magnetic field data at two different heights are also used, were also submitted to these test data. We used two series of these data.

The first series was the "flower" data, where the sunspots are simulated with form of flowers, as visible in Fig. 4 of Leka et al. (2009). These data were prepared to test the code robustness against lack of spatial resolution. The preparation of the theoretical data is described in p. 93 of Leka et al. (2009) and also in p. 111 of Crouch (2013). We used the theoretical data with averaged pixel sizes of 0.3" and 0.9". These theoretical data are provided at two heights separated by 0.18". These data simulate location at disk center, i.e., the line-of-sight is assumed to be perpendicular to the line formation planes. For these data, we obtained the result metrics listed in Table 1. The metrics is given by the fraction of pixels with correct ambiguity resolution in the whole map $\mathcal{M}_{\text{area}}$ and the fraction of pixels with correct ambiguity resolution within the conditions of transverse field $H_\perp$ stronger than 100 G and 500 G respectively. As visible in Table 1, our code obtains excellent results for the two resolution cases.

The second series of data was the simulation represented in Fig. 1 of Leka et al. (2009). These data were artificially noised by adding them a theoretical photon noise, at the level of polarimetric accuracy of 10^{-3} for the low noise case and 10^{-2} for the high noise case, as described in p. 89 of Leka et al. (2009). The assumed pixel size was 0.5". The case without any added noise was also treated. These data are available at two heights. We used data at two heights distant of 890 km along the l.o.s., whereas Crouch (2013) used data at two heights distant of the pixel size as described in p. 111 of Crouch (2013), which is 376 km only. For these data, we obtained the result metrics listed in Table 2. In this case also, our code obtains very good results. The results are perfect in the case without any noise. The highest noise level, which is 10^{-2} in polarization, is rather high and higher than the current observation polarization inaccuracies. In the case of this high level noise, we obtain nevertheless rather good results better than 80% correct for the high noise level and better than 95% correct for the low noise level. As visible in Table 2, our worst results locate in weak magnetic field regions.

This second series of data were assumed to be located out of disk center at latitude 9° South and longitude 36° East with respect to the central meridian. This leads to an heliocentric angle cosine $\mu = \cos\theta = 0.80$, which is rather far from disk center. It has to be remarked that we obtain perfect ambiguity resolution result with our code in the no noise case as visible in the first line of Table 2. In our code, the disambiguation is performed in the l.o.s. reference frame and we applied Eq. (10) to account for departure from disk center in the case of lines formed along horizontal planes, which is done in the second line of Eq. (10). The success of our resolution of theoretical data again validates our Eq. (10) and, in particular, its second line in the case of lines formed along horizontal planes and observed out of disk center.

4. Results: Examples of Vector Maps

The results presented below were obtained from 86 maps observed with THÉMIS and 23 maps observed by HINODE/SOT/SP, which are visible in V. Bommier's personal page[3]. The magnetic field final values are also available on-line there. Four examples of HINODE data and two examples of THÉMIS data are included in Figs. 4-11 below. For accuracy reasons, the HINODE data pixels were two times binned two by two before the ambiguity resolution, which results in pixel sizes of $\Delta x = 862$ km and $\Delta y = 928$ km. This was also done for the tests described in the following Sect. 5. The THÉMIS data pixel
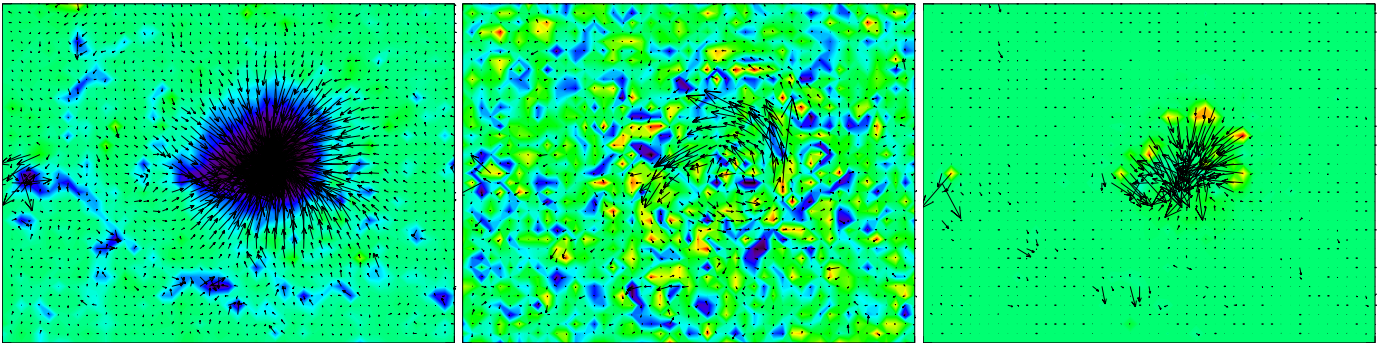

[3] http://lesia.obspm.fr/perso/veronique-bommier

Fig. 4. Active Region NOAA 11420 observed by HINODE/SOT/SP on 18 February 2012 between 11:08 and 12:04 UT. The ambiguity is resolved by our method. Left: magnetic field vector, vertical component between −2040 and +2040, horizontal component maximum arrow length 1355 G. Middle: current density vector, vertical component between −64 and +64, horizontal component typical arrow length 5000 mA/m^2. Right: Lorentz force vector, vertical component between −448 and +448 , horizontal component typical arrow length 800 mN/m^2. The spatial resolution was reduced by a factor 5 × 5 for paper file size purposes. (color figure on-line)
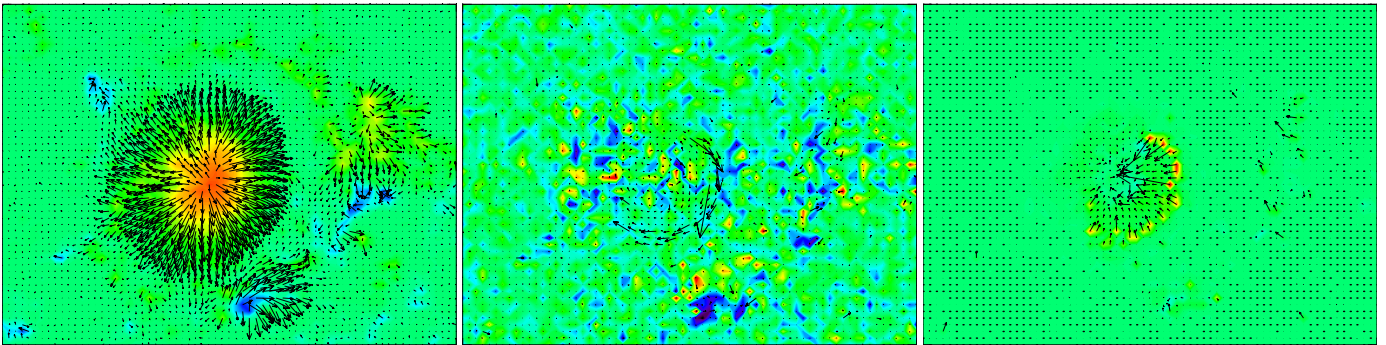
Fig. 5. Active Region NOAA 11494 observed by HINODE/SOT/SP on 7 June 2012 between 14:15 and 15:05 UT. The ambiguity is resolved by our method. Left: magnetic field vector, vertical component between −2150 and +2150, horizontal component maximum arrow length 1743 G. Middle: current density vector, vertical component between −219 and +219, horizontal component typical arrow length 5000 mA/m^2. Right: Lorentz force vector, vertical component between −682 and +682 , horizontal component typical arrow length 800 mN/m^2. The spatial resolution was reduced by a factor 5 × 5 for paper file size purposes. (color figure on-line)
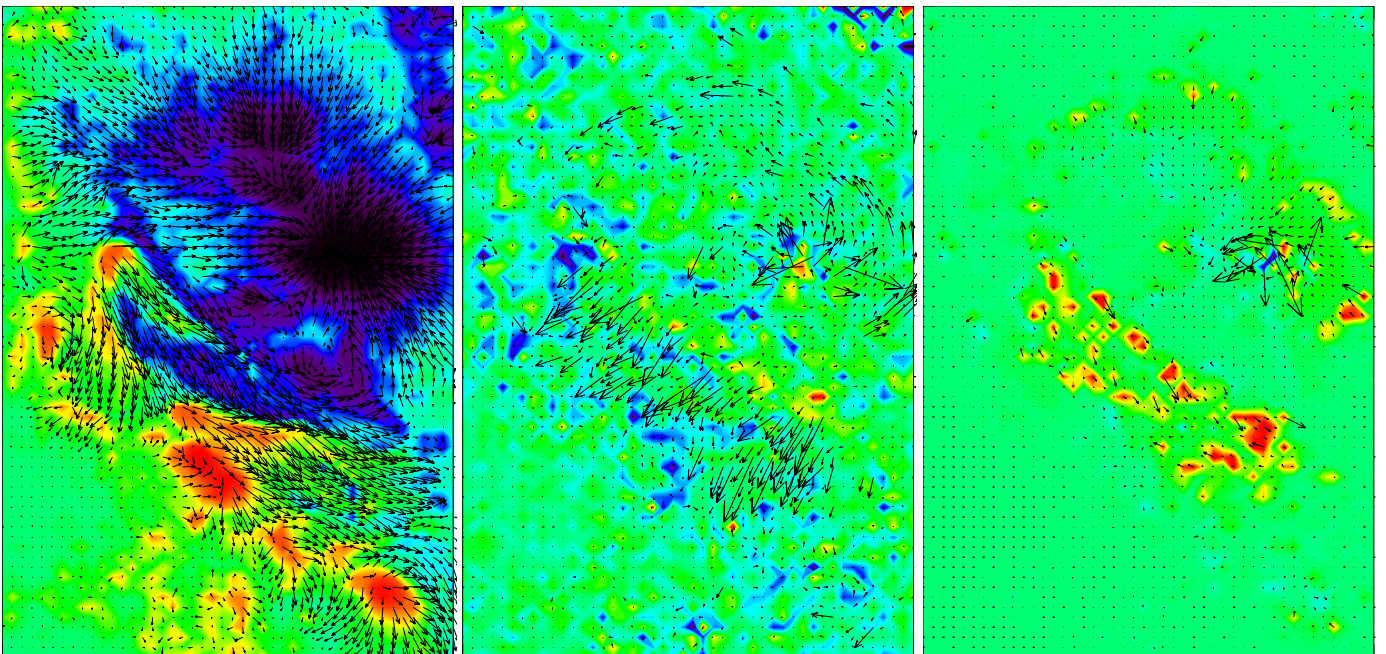

Fig. 6. Active Region NOAA 11476 observed by HINODE/SOT/SP on 12 May 2012 between 02:38 and 03:11 UT. The ambiguity is resolved by our method. Left: magnetic field vector, vertical component between −2450 and +2450, horizontal component maximum arrow length 2470 G. Middle: current density vector, vertical component between −218 and +218, horizontal component typical arrow length 8000 mA/m^2. Right: Lorentz force vector, vertical component between −1040 and +1040 , horizontal component typical arrow length 800 mN/m^2. The spatial resolution was reduced by a factor 5 × 5 for paper file size purposes. (color figure on-line)
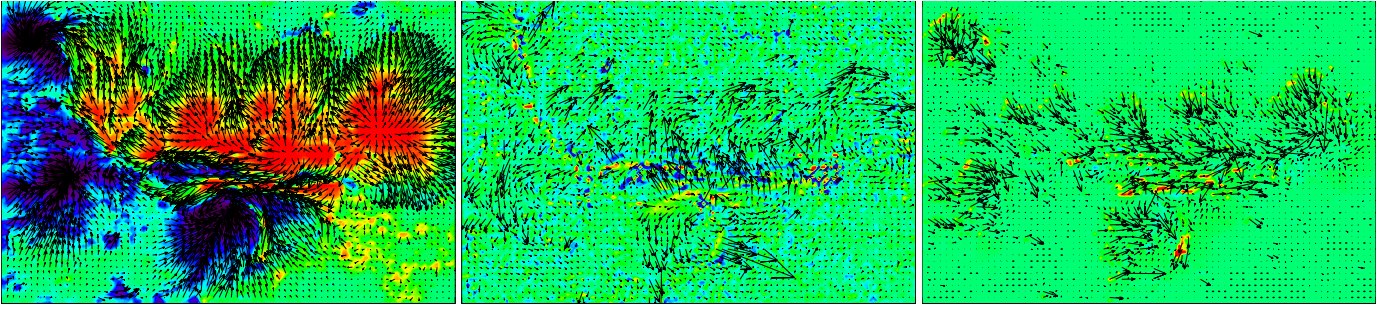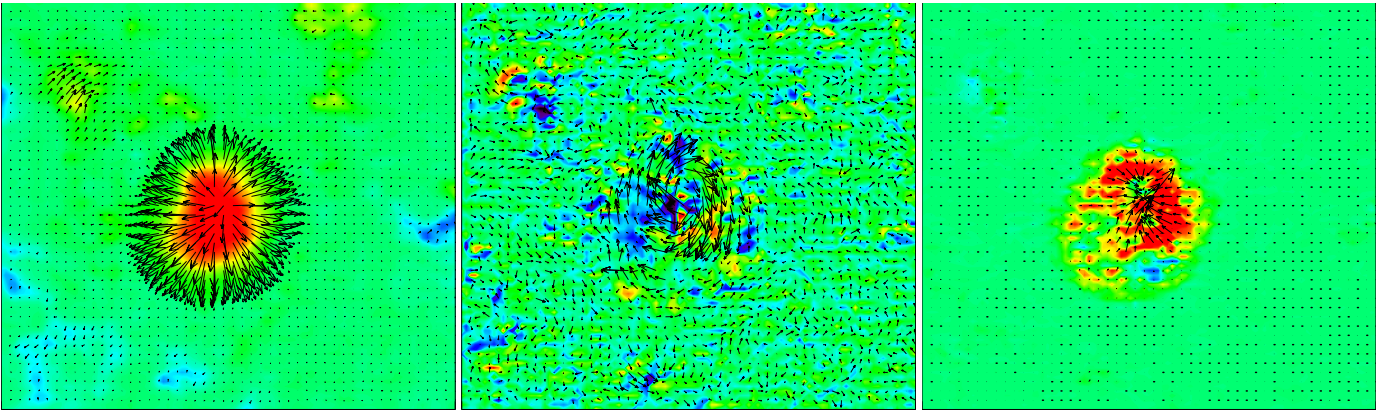
Fig. 7. Active Region NOAA 11429 observed by HINODE/SOT/SP on 6 March 2012 between 22:10 and 22:43 UT. The ambiguity is resolved by our method. Left: magnetic field vector, vertical component between −2480 and +2480, horizontal component maximum arrow length 2441 G. Middle: current density vector, vertical component between −185 and +185, horizontal component typical arrow length 5000 mA/m^2. Right: Lorentz force vector, vertical component between −1180 and +1180 , horizontal component typical arrow length 800 mN/m^2. The spatial resolution was reduced by a factor 5×5 for paper file size purposes. (color figure on-line)

Fig. 8. Active Region NOAA 11857 observed with THEMIS on 7 October 2013 between 08:57 and 09:22 UT, in the photospheric lines Fe I 6301/6302. The ambiguity is resolved by our method. Left: magnetic field vector, vertical component between −1790 and +1790, horizontal component maximum arrow length 1070 G. Middle: current density vector, vertical component between −68 and +68, horizontal component maximum arrow length 746 mA/m^2. Right: Lorentz force vector, vertical component between −56 and +56 , horizontal component maximum arrow length 133 mN/m^2. (color figure on-line)
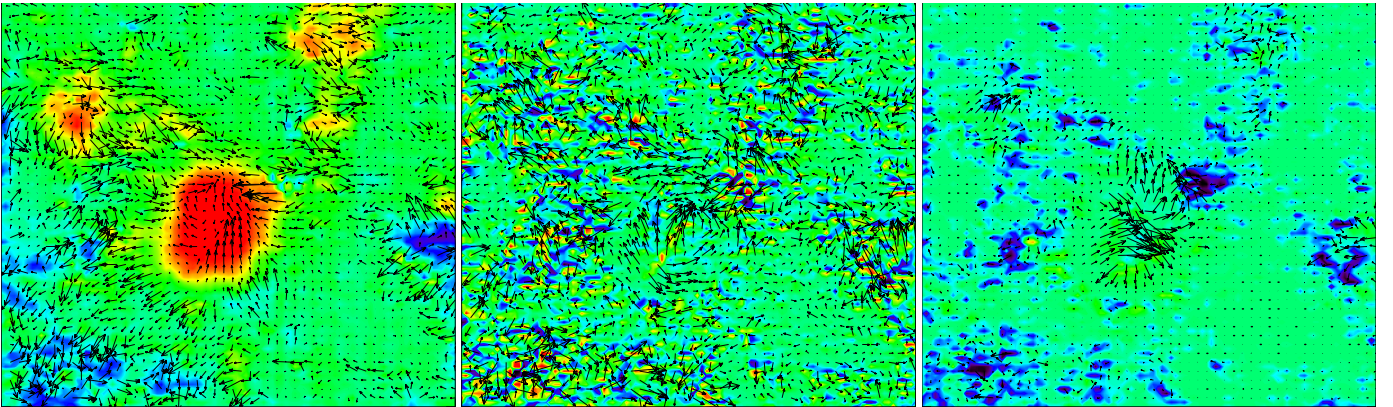

Fig. 9. Active Region NOAA 11857 observed with THEMIS on 7 October 2013 between 09:24and 10:42 UT, in the chromospheric lines Na I D1/D2. The ambiguity is resolved by our method. Left: magnetic field vector, vertical component between −772 and +772, horizontal component maximum arrow length 1254 G. Middle: current density vector, vertical component between −188 and +188, horizontal component maximum arrow length 1495 mA/m^2. Right: Lorentz force vector, vertical component between −155 and +155 , horizontal component maximum arrow length 54 mN/m^2. (color figure on-line)

size was $\Delta x = 794$ km and $\Delta y = 725$ km, the binning was not performed.

4.1. HINODE data: examples of a single regular spot

We systematically observe a strong circular horizontal current component, which wraps spots clockwise about a positive polarity spot and anticlockwise about a negative polarity spot. As a consequence, the Lorentz force vector is systematically found centripetal with respect to the spot center. Numerous examples
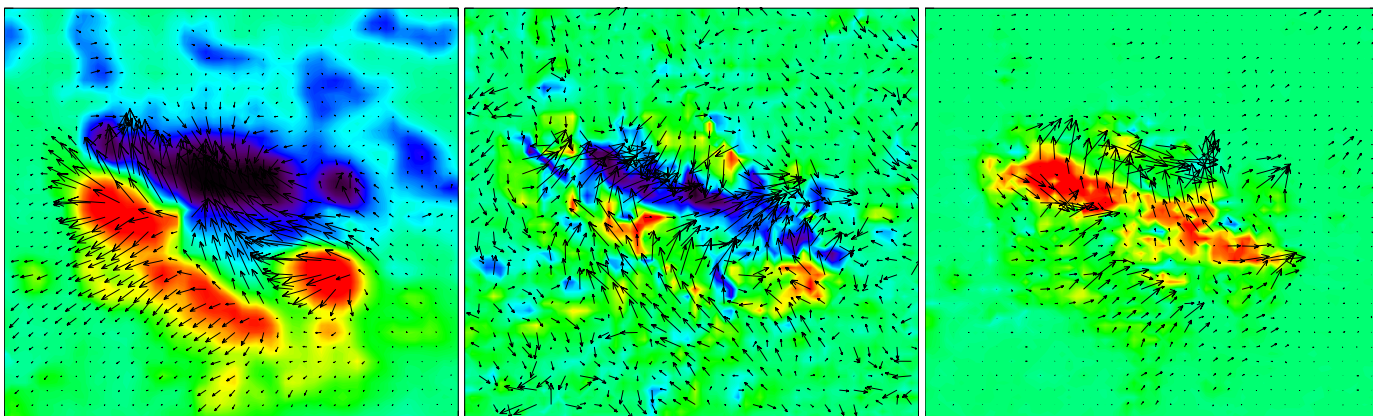
Fig. 10. Active Region NOAA 11865 observed with THEMIS on 11 October 2013 between 09:39 and 09:59 UT, in the photospheric lines Fe I 6301/6302. The ambiguity is resolved by our method. Left: magnetic field vector, vertical component between −1450 and +1450, horizontal component maximum arrow length 1320 G. Middle: current density vector, vertical component between −96 and +96, horizontal component maximum arrow length 655 mA/m^2. Right: Lorentz force vector, vertical component between −83 and +83 , horizontal component maximum arrow length 43 mN/m^2. (color figure on-line)
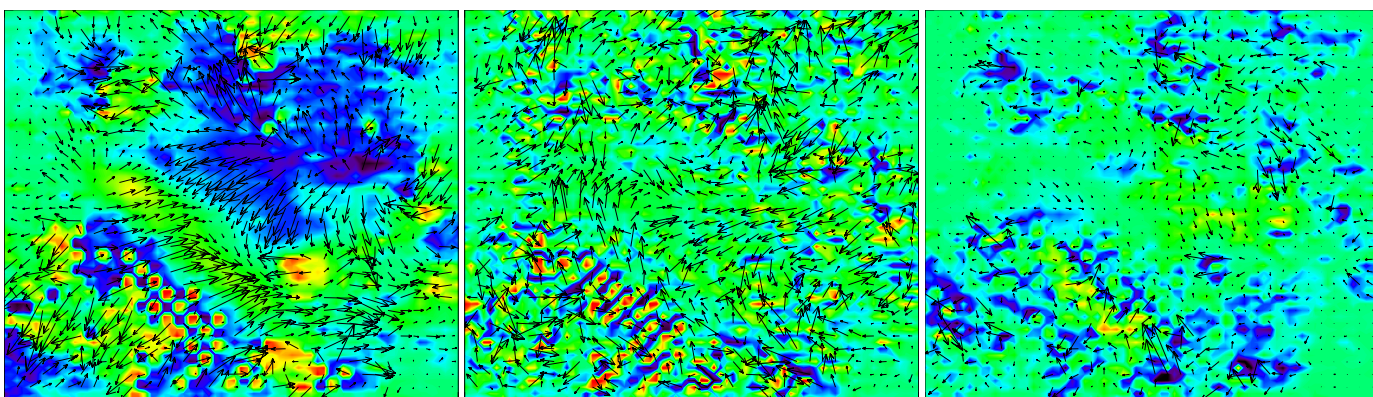

Fig. 11. Active Region NOAA 11865 observed with THEMIS on 7 October 2013 between 10:14 and 11:19 UT, in the chromospheric lines Na I D1/D2. The ambiguity is resolved by our method. Left: magnetic field vector, vertical component between −930 and +930, horizontal component maximum arrow length 979 G. Middle: current density vector, vertical component between −148 and +148, horizontal component maximum arrow length 1127 mA/m^2. Right: Lorentz force vector, vertical component between −79 and +79 , horizontal component maximum arrow length 59 mN/m^2. (color figure on-line)

can be found along the web page. We can cite in particular the active regions NOAA 11420 observed by HINODE/SOT/SP on 18 February 2012 between 11:08 and 12:04 UT (negative polarity spot), which is represented in Fig. 4, and NOAA 11494 observed by HINODE/SOT/SP on 7 June 2012 between 14:15 and 15:05 UT (positive polarity spot), which is represented in Fig. 5. These examples can be found in the web page with a better spatial resolution. Similar examples can be found in the web page for HINODE/SOT/SP observations of single spots on 12 December 2006, 7 September 2011, 1 February 2012, 1 May 2012, and 13 June 2012.

4.2. HINODE data: examples of a neutral line

We often observe a strong horizontal current component, which crossesthe neutral line. Two examples are presented in this paper, which can also be found in the web page: NOAA 11476 observed by HINODE/SOT/SP on 12 May 2012 between 02:38 and 03:11 UT, which is represented in Fig. 6, and NOAA 11429 observed by HINODE/SOT/SP on 6 March 2012 between 22:10 and 22:43, which is represented in Fig. 7. One can refer to the web page for a better spatial resolution. NOAA 11476, which is represented in Fig. 6, produced numerous C-class flares and

NOAA 11429, which is represented in Fig. 7, produced an X-class flare followed by a CME. The example of 7 September 2011, which is visible in the web page, is also the case of an active region that produced an X-class flare. A strong horizontal current component is well visible across the neutral line.

4.3. THÉMIS data: example of a single regular spot

The example presented in this paper is the case of NOAA 11857 observed with THÉMIS on 7 October 2013, between 08:57 and 09:22 UT in Fe I 6301/6302, between 09:24 and 09:59 UT in Na I D2 and between 10:10 and 10:42 UT in Na I D1. In the case of the photosphere, which is observed in Fe I 6301/6302 and is represented in Fig. 8, we find again the current and Lorentz force characteristics described above, namely circular current about the spot and centripetal Lorentz force. Higher, at the low chromosphere level, which is observed in Na I D1/D2 and is represented in Fig. 9, the field and current organizations are found more complex. We observe, however, a good agreement between the photospheric and chromospheric magnetic fields, which leads us to think that the ambiguity was correctly resolved at the chromospheric level observed with the Na I D lines. NOAA 11857 was observed with THÉMIS in both iron

and sodium lines on 5 October, 7 October (two times, morning and afternoon), 8 October, and 9 October. All these examples are visible in the web page. The magnetic field is more rotating about the spot center at the chromospheric level than at the photospheric level, where it is more radial.

4.4. THÉMIS data: example of a neutral line

The example presented in this paper is the case of NOAA 11865 observed with THÉMIS on 11 October 2013, between 09:39 and 09:59 UT in Fe I 6301/6302, between 10:14 and 10:43 UT in Na I D2, and between 10:50 and 11:19 UT in Na I D1. Again, in the photosphere, which is observed in Fe I 6301/6302 and is represented in Fig. 10, we observe a strong horizontal current component across the neutral line. The structure of the currents is more involved at the low chromosphere level, which is observed in Na I D1/D2 and is represented in figure 11.

5. Verification: comparison with results obtained by applying available codes

In order to check our method, we applied different available codes for ambiguity resolution to our data.

5.1. Case of the 1-line Metcalf ME0 code applied to each line

First, we applied the Metcalf ME0 code described by Leka et al. (2009) to each line map. This code is able to resolve the ambiguity by using only one line data. For computing the magnetic field divergence for minimization, the horizontal derivatives are computed from the data, whereas the vertical derivative is derived from a current-free extrapolation from the data. The departure from disk center is accounted for as explained in Crouch et al. (2009). This code does not apply the scaling by the aspect ratio that we propose in Sect. 3.5 and we did not modify this point. This is not necessary because the extrapolation step is performed within the divergence-free condition. We did not at all modify the code.

We applied the code independently to each of the two Fe I 6301.5 Å and 6302.5 Å lines of our HINODE/SOT/SP observations of Figs. 4-7. We then plotted the current density vector by computing it from the two line magnetic field maps, by assuming a depth difference of 66 km between the two lines following Sect. 3.4. The results are given in Fig. 12, where it can be seen that the direction of the current density vector well matches the one we obtained with our method and given in Figs. 4-7. In particular, the direction of the spot wrapping current is fully recovered, together with the way how the current density vector crosses the neutral line. We then infer that our ambiguity resolution was correct. However, it can be seen that the result is more noisy with the ME0 resolution method thus applied.

5.2. Case of the two-line AMBIG2 code proposed by Crouch (2013)

We then applied the two-line code AMBIG2 proposed by Crouch (2013)[4], who presented runs on theoretical data. We applied it to our real data represented in Figs. 4-7. For a better comparison, we ran the code in the conditions of Eq. (8) of Crouch (2013), which are the closest conditions to those we applied as described in Sect. 3.3. As in our resolution code, we assigned a value of 98

---

[4] http://www.cora.nwra. com/~ash/ambig2.tar.gz

km to the two line depth difference, which is a bit higher than the 66 km value described above in Sect. 3.4 because this last value was obtained in quiet Sun conditions, whereas our data concern a sunspot. It can be seen in Figure 4 of Khomenko & Collados (2007) that the two Fe I 6301.5 Å and 6302.5 Å formation depth difference is a bit higher in active regions. The depth difference value was corrected from the disk center departure.

As mentioned in Sect. 3.6, the ambiguity solution is intuitively known in sunspots from their polarity. This enables a verification procedure. We applied the code to our HINODE/SOT/SP data of Fig. 4. The results for comparison are displayed in Fig. 13, where it can be seen that the ambiguity solution does not correspond to the spot polarity inside a zone located South-West (i.e., bottom-right) from the spot center.

For comparison, we then simulated our aspect ratio scaling described in Sect. 3.5 without modifying the code, by artificially dividing by 10 the x and y pixel sizes. The spot was located at longitude $-8°$ from the central meridian and latitude $23°$. As a result, the heliospheric angle was $24°$ with cosine $\mu = 0.91$. The spot was not so far from disk center. Therefore, the above described simulation of the aspect ratio scaling was sufficient without any other modification and in particular not any code modification. The results are plotted in Fig. 14, where it can be seen that now the ambiguity solution well matches the spot polarity in the whole map. The success of the ambiguity resolution when the scaling by the aspect ratio is applied as in Fig. 14, whereas the resolution is unsuccessful when the scaling by the aspect ratio is not applied as in Fig. 13, confirms our conviction about the necessity of applying this aspect ratio scaling to vanish the magnetic field divergence in the data following our analysis in Bommier (2013, 2014) and recalled in Sect. 3.5.

The current density vector directions obtained are also in full agreement with the directions we obtained with our method. This is in particular the case of the direction of the spot wrapping current. This also validates our ambiguity resolution.

The same analysis was applied with the same results to the data corresponding to Figs. 5-7. No map was successfully resolved without the scaling. For the data of Fig. 5 and Fig. 7, the ambiguity resolution was successful when the applied scaling factor was 20 instead of 10, which exactly matches the theoretical aspect ratio we derived for the photosphere in Bommier (2013, 2014). For the data of Fig. 6, it was not possible to get a correct ambiguity resolution whatever the applied scaling factor is. These analyses on several cases confirm our intuition that the theoretical value of 20 for the scaling factor has to be considered more as an order of magnitude than as a well-defined value, as previously stated in Sect. 3.5.

One of the main results of the present paper is the necessity to apply the scaling factor to the data before disambiguation. This can be done in an external way by artificially dividing the pixel sizes before sumbission to the AMBIG2 code, provided that the observed region is located close to disk center. Our disambiguation code is able to also disambiguate data of regions located out of disk center because departure from disk center is fully integrated into Eq. (10).

6. Conclusion

We have shown that observations in two different lines, which belong to the same multiplet but have different absorption coefficients so that they are formed at two different depths, like Fe I 6302.5 Å and 6301.5 Å, enable the resolution of the azimuth ambiguity, which remain from the Zeeman signal interpretation. The anisotropy of the strongly stratified plasma of the
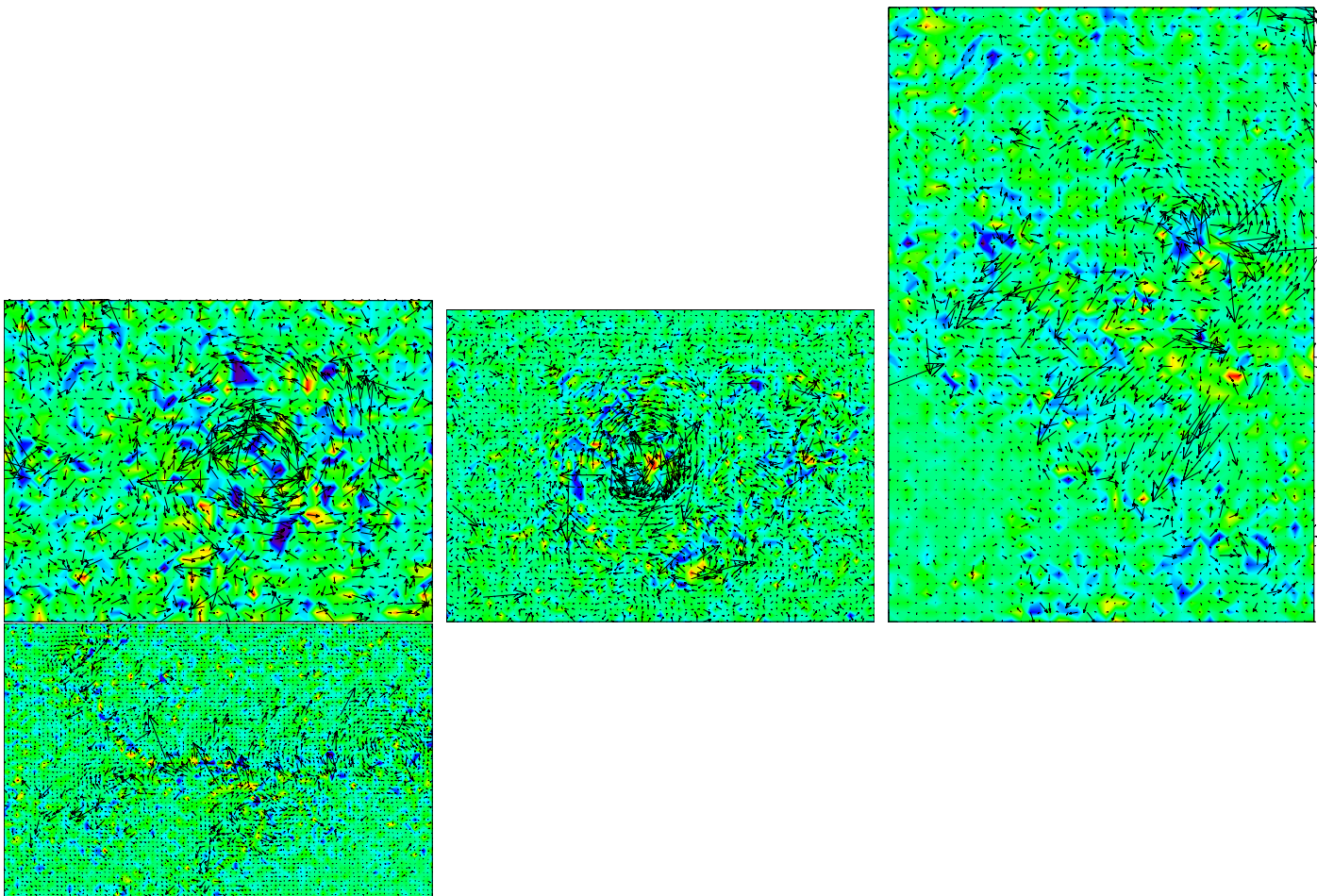
Fig. 12. Current vector maps of the four active regions of Figs. 4-7, but the ambiguity is resolved by another method. The ambiguity is resolved independently for each line map by applying the Metcalf ME0 code (Leka et al. 2009). The current vector is then plotted by assuming the depth difference 66 km (see Sect. 3.4), corrected for the disk center departure, between the two line maps.
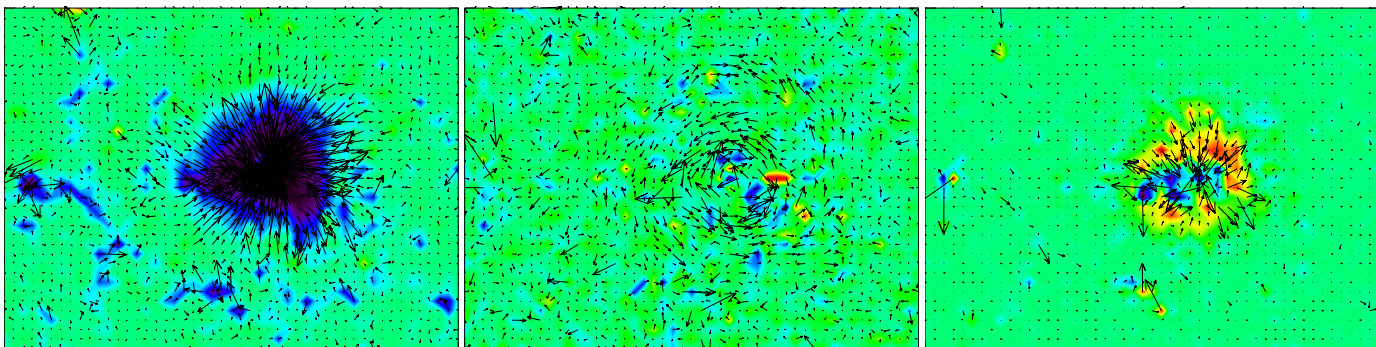

Fig. 13. Same as Fig. 4, but the ambiguity is resolved by applying the two line code by Crouch (2013) in the conditions corresponding to Eq. (8) of that paper. The ambiguity resolution solution is not in agreement with the spot polarity in a zone South-West (i.e., bottom-right) of the spot center. (color figure on-line)

photosphere has also to be accounted for following Bommier (2013) and Bommier (2014). As a consequence, two ambiguity-resolved field vector maps are obtained at two different but close altitudes, which enable the derivation of the current density full vector via rot $\boldsymbol{H} = \boldsymbol{J}$. This reveals the horizontal component of the current density, which is found markedly stronger than the better known vertical one, as already observed by Puschmann et al. (2010) from HINODE/SOT/SP data. We observe some systematical trends, like circular currents wrapping spots clockwise about a positive polarity spot and anticlockwise about a negative

polarity spot and strong horizontal current components, which cross active region neutral lines. The wrapping direction with respect to the spot polarity is the same as the average one in Fig. 1 of Puschmann et al. (2010), who applies completely different methods. As a result, the Lorentz force may be computed. It is found to be centripetal in sunspots.

We successfully compared the results of our method to the results of other codes based on other methods and applied to the same observation data. In particular, we applied the publicly available AMBIG2 code by Crouch (2013) to our real solar data.
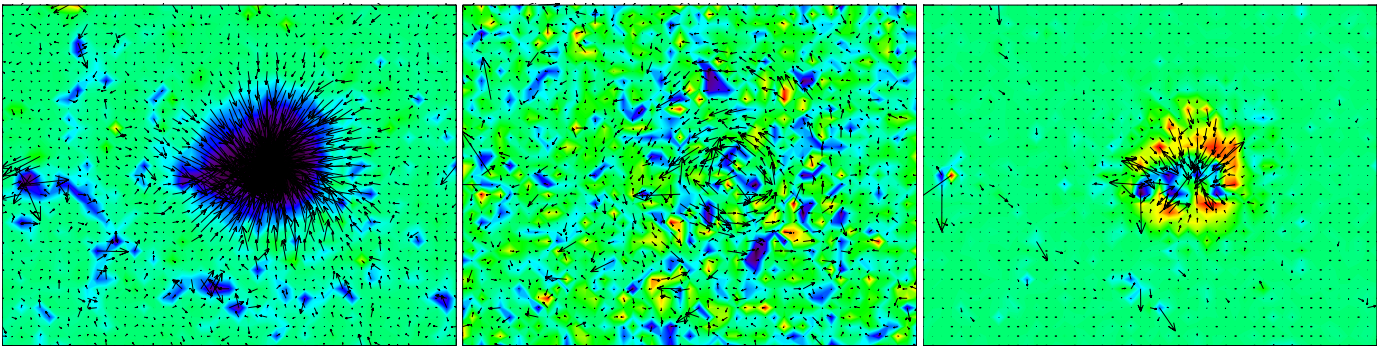
Fig. 14. Same as Fig. 13, but our proposed scaling has been applied without modifying the ambiguity resolution code, by artificially dividing by 10 the x and y pixel size in the image plane. The ambiguity resolution solution is now in agreement with the spot polarity in the whole map. (color figure on-line)

We obtained that the anisotropic scaling of the real solar data following the aspect ratio in the strongly stratified medium of the solar photosphere, suggested by Bommier (2013) and Bommier (2014), has to be applied for a correct resolution of the ambiguity. The correctness can be established by comparison with the intuitive ambiguity solution, which can be derived in spot penumbrae from the spot polarity. The necessity of applying the aspect ratio for solving the ambiguity is another main result of the present work.

We finally remarked that the Na I D1 and D2 lines form another such line pair. We successfully tested their application to full vector mapping of the magnetic field and current density with THÉMIS telescope observation. Observing this line pair would open access to the low chromosphere where they are formed.

References

Balthasar, H. 2018, Sol. Phys., 293, 120

Bommier, V. 2013, Physics Research International, 2013, 195403

Bommier, V. 2014, Comptes Rendus Physique, 15, 430

Bommier, V. 2015, in IAU Symposium, Vol. 305, Polarimetry, ed. K. N. Nagendra, S. Bagnulo, R. Centeno, & M. Jesús Martínez González, 28–34

Bommier, V. 2020, A&A, 634, A40

Bommier, V., Landi Degl'Innocenti, E., Landolfi, M., & Molodij, G. 2007, A&A, 464, 323

Bommier, V., Landi Degl'Innocenti, E., & Sahal-Bréchot, S. 1991, A&A, 244, 383

Brethouwer, G., Billant, P., Lindborg, E., & Chomaz, J. M. 2007, Journal of Fluid Mechanics, 585, 343

Bruls, J. H. M. J., Lites, B. W., & Murphy, G. A. 1991, in Solar Polarimetry, Proceedings of the 11st National Solar Observatory/Sacramento Peak Summer Workshop, Sunspot, New Mexico, 27-31 August 1990, ed. L. J. November (National Solar Observatory), 444–456

Crouch, A. D. 2013, Sol. Phys., 282, 107

Crouch, A. D. 2015, Sol. Phys., 290, 2677

Crouch, A. D., Barnes, G., & Leka, K. D. 2009, Sol. Phys., 260, 271

Fan, Y. & Gibson, S. E. 2004, ApJ, 609, 1123

Faurobert, M., Aime, C., Périni, C., et al. 2009, A&A, 507, L29

Gary, G. A. & Hagyard, M. J. 1990, Sol. Phys., 126, 21

Grec, C., Uitenbroek, H., Faurobert, M., & Aime, C. 2010, A&A, 514, A91

Khomenko, E. & Collados, M. 2007, ApJ, 659, 1726

Landi Degl'Innocenti, E. 1976, A&AS, 25, 379

Landi Degl'Innocenti, E., Bommier, V., & Sahal-Bréchot, S. 1990, A&A, 235, 459

Landolfi, M. & Landi Degl'Innocenti, E. 1982, Sol. Phys., 78, 355

Landolfi, M., Landi Degl'Innocenti, E., & Arena, P. 1984, Sol. Phys., 93, 269

Leka, K. D., Barnes, G., Crouch, A. D., et al. 2009, Sol. Phys., 260, 83

Leka, K. D., Fan, Y., & Barnes, G. 2005, ApJ, 626, 1091

Leka, K. D., Wagner, E. L., Griñón-Marín, A. B., Bommier, V., & Higgins, R. E. L. 2022, Sol. Phys., 297, 121

Maltby, P., Avrett, E. H., Carlsson, M., et al. 1986, ApJ, 306, 284

Metcalf, T. R. 1994, Sol. Phys., 155, 235

Metcalf, T. R., Leka, K. D., Barnes, G., et al. 2006, Sol. Phys., 237, 267

Molodij, G., Bommier, V., & Rayrole, J. 2011, A&A, 531, A139

Puschmann, K. G., Ruiz Cobo, B., & Martínez Pillet, V. 2010, ApJ, 721, L58

Ruiz Cobo, B. & del Toro Iniesta, J. C. 1992, ApJ, 398, 375

Socas-Navarro, H. 2005, ApJ, 633, L57

Stenflo, J. O. 1973, Sol. Phys., 32, 41

Vernazza, J. E., Avrett, E. H., & Loeser, R. 1973, ApJ, 184, 605

Appendix A: Expressions of the divergence and curl when the quantities are measured along an inclined line formation plane

We describe below how divergence and curl have to be computed, when the measurements are made in pixels, and when the spectral line used for the measurements is formed at a certain depth in the stellar atmosphere. This depth defines a formation plane for the line. In the following we neglect an eventual thickness of this plane, which we consider as infinitely sharp. We consider the general case where this plane is inclined with respect to the line-of-sight for an observation performed out of disk center. The case of disk center observation is however possible as a particular case.

We denote the heliographic reference frame as $OXYZ$ and the l.o.s. reference frame as $Oxyz$ with Oy solar north oriented. The point O where divergence and curl are computed is taken at longitude-latitude (L, b). The solar radius unit vector $\boldsymbol{R}$ in O is perpendicular to the the line formation plane, which is tangent to the solar surface. The $\boldsymbol{R}$ coordinates in the l.o.s. reference frame are given in Eq. (2). In the l.o.s. reference frame, the line formation plane, which is perpendicular to $\boldsymbol{R}$ of coordinates (R_x, R_y, R_z), has then for general equation

$$R_x x + R_y y + R_z z = 0 . \tag{A.1}$$

Let's denote as $\boldsymbol{H}^{(1)}$ the magnetic field vector measured as a function of x and y along the formation plane of the line number (1). $\boldsymbol{H}^{(1)}$ depends on the following variables

$$\boldsymbol{H}^{(1)}(x, y, z; R_x x + R_y y + R_z z = 0) , \tag{A.2}$$

where the semicolon means "such as". A similar law holds for the magnetic field vector $\boldsymbol{H}^{(2)}$ measured with the second line number (2). In the l.o.s. reference frame $Oxyz$, we denote as Δx and Δy the distance between two neighboring pixels along the Ox and Oy axes respectively in the "sky plane". Let's denote as $\Delta_x H_x^{(1)}$ the variation of $H_x^{(1)}$ between two neighboring pixels in x direction $(i + 1, j)$ and (i, j) distant of Δx in the image

$$\Delta_x H_x^{(1)} = H_x^{(1)}(i + 1, j) - H_x^{(1)}(i, j) , \tag{A.3}$$

and analogously

$$\Delta_y H_y^{(1)} = H_y^{(1)}(i, j + 1) - H_y^{(1)}(i, j) . \tag{A.4}$$

For the second line one can similarly define $\Delta_x H_x^{(2)}$ and $\Delta_y H_y^{(2)}$. The magnetic field may be averaged between the two lines, with the acute angle method when the ambiguity is not resolved, and in this case we denote the average as $\Delta_x H_x^{(m)}$ and $\Delta_y H_y^{(m)}$. As for the z variation, it involves the two lines as

$$\Delta_z H_z^{(m)} = H_z^{(1)}(i, j) - H_z^{(2)}(i, j) . \tag{A.5}$$

Appendix A.1: Calculation of the divergence

The mathematical expression of div $\boldsymbol{H}$ is frame-independent

$$\text{div } \boldsymbol{H} = \frac{\partial H_x}{\partial x} + \frac{\partial H_y}{\partial y} + \frac{\partial H_z}{\partial z} . \tag{A.6}$$

However, a problem arises when it is discretized in the above described system of line formation planes. $\Delta_x H_x^{(1)}/\Delta x$, which could a priori be considered as the $\partial H_x/\partial x$ contribution, includes also a variation of $H_x^{(1)}$ along the Oz axis because the magnetic field is measured along the line formation plane. As a consequence,
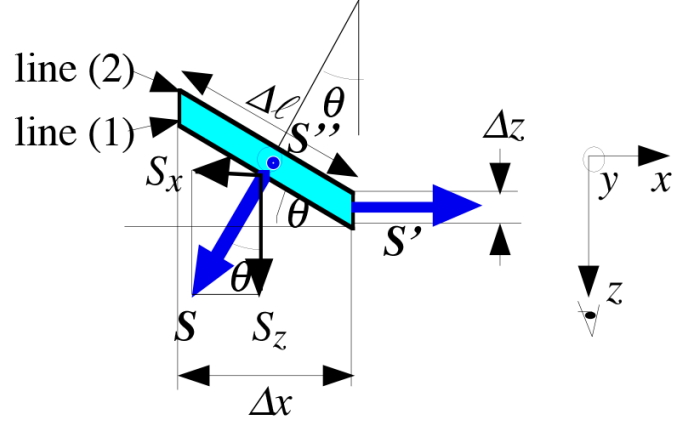
Fig. A.1. Reference frame for the divergence evaluation: case of an observation at the solar equator. The heliocentric θ angle is oriented by the Oy axis and is negative in the figure. The two formation planes corresponding to the two lines (1) and (2) are indicated by their respective number. The unit S vector is indeed the same as the unit R vector along the local solar radius.

$\Delta_x H_x^{(1)}/\Delta x$ cannot finally be considered as an approximation of $\partial H_x/\partial x$ because $\partial H_x/\partial x$ is the variation of H_x with x at constant y and z following the mathematical definition.

The present Appendix is devoted to account for this difficulty by applying the Ostrogradski's theorem, which is that the volume integrated divergence equals the flux of the quantity through the surface that borders the volume. We apply this theorem to the small volume delineated by four neighboring pixels separated by Δx and Δy in the sky plane xOy but located in the line formation plane, and the corresponding four other pixels for the second line formed in another formation plane separated from the first one by the distance Δz along the line-of-sight. In the following we detail three different derivations from the simplest to the most complex. We consider first an observation located at the solar equator without inclination of the solar rotation axis (Sect. A.1.1). We then generalize this demonstration to the general case (Sect. A.1.2) and we add a more elegant derivation leading to the same result as a third part (Sect. A.1.3).

Appendix A.1.1: Case of a region located at solar equator

We first assume that O is located on solar equator and that the Sun rotation axis lies in the plane of the sky, i.e. that $b_0 = 0$. The heliocentric angle is denoted as θ. A section of the small volume introduced above is represented in Fig. A.1. For each side of the volume, a unit vector perpendicular to the surface and pointing towards the exterior of the volume can be plotted. Three of these vectors are plotted in Fig. A.1, $\boldsymbol{S}$, $\boldsymbol{S}'$, and $\boldsymbol{S}''$. One has to calculate the flux of the magnetic field through each elementary surface. Consider first the surface element associated to the $\boldsymbol{S}$ vector. This surface element is part of the formation plane of line number (1), whereas $\boldsymbol{S}'$ and $\boldsymbol{S}''$ join the two line formation planes. In the l.o.s. reference frame $Oxyz$, the $\boldsymbol{S}$ unit vector has the following coordinates

$$\boldsymbol{S} \begin{cases} S_x = \sin\theta \\ S_y = 0 \\ S_z = \cos\theta \end{cases} . \tag{A.7}$$

As a consequence, the flux of the magnetic field through this surface per surface unit is

$$\boldsymbol{H}^{(1)} \cdot \boldsymbol{S} = H_z^{(1)} \cos\theta + H_x^{(1)} \sin\theta . \tag{A.8}$$
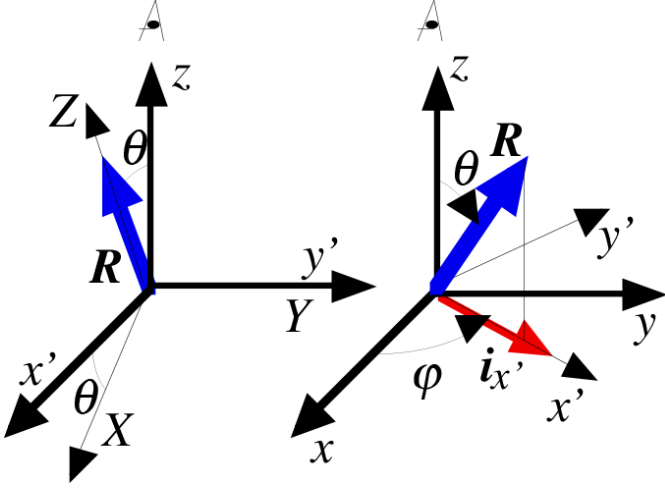
Fig. A.2. Reference frame for the divergence evaluation: general case.

As visible in Fig. A.1, the elementary surface value is $\Delta\ell\Delta y$, where

$$\Delta\ell = \frac{\Delta x}{\cos\theta} \, . \tag{A.9}$$

The flux through this elementary surface is then finally

$$\boldsymbol{H}^{(1)} \cdot \boldsymbol{S} \, \Delta\ell\Delta y = (H_z^{(1)} + H_x^{(1)}\tan\theta)\,\Delta x\Delta y \, . \tag{A.10}$$

The flux through the elementary surface associated to $\boldsymbol{S}'$ is

$$\boldsymbol{H}^{(m)} \cdot \boldsymbol{S}' \, \Delta z\Delta y = H_x^{(m)}\Delta z\Delta y \, , \tag{A.11}$$

where the superscript (m) denotes the average between the two lines (1) and (2). Finally, the flux through the third elementary surface $\boldsymbol{S}''$ is

$$\boldsymbol{H}^{(m)} \cdot \boldsymbol{S}'' \, \Delta\ell\Delta z \cos\theta = H_y^{(m)}\Delta x\Delta z \, . \tag{A.12}$$

As the elementary volume is $\Delta\ell\Delta y\Delta z\cos\theta = \Delta x\Delta y\Delta z$, one has finally in application of Ostrogradski's theorem

$$
\begin{aligned}
&\mathrm{div}\,\boldsymbol{H}\,\Delta x\Delta y\Delta z \\
&= \left[(H_z^{(1)} - H_z^{(2)}) + (H_x^{(1)} - H_x^{(2)})\tan\theta\right]\Delta x\Delta y \\
&+ \left[H_x^{(m)}(x + \Delta x, y) - H_x^{(m)}(x, y)\right]\Delta z\Delta y \\
&+ \left[H_y^{(m)}(x, y + \Delta y) - H_y^{(m)}(x, y)\right]\Delta x\Delta z \, ,
\end{aligned}
\tag{A.13}
$$

which results in Eq. (11) of the paper. The term in $\tan\theta$ accounts for the line formation plane inclination with respect to the line-of-sight.

Appendix A.1.2: Generalization

One considers now a point O on the solar surface with longitude L and latitude b. The solar radius in O denoted as $\boldsymbol{R}$ is perpendicular to the line formation plane. The $\boldsymbol{R}$ coordinates in terms of (L, b) are given in Eq. (2). There is a common perpendicular to this radius R and to the l.o.s. Oz. We denote as $Oy' = OY$ this common perpendicular, which is represented in the left part of Fig. A.2. In this section, the $OXYZ$ reference frame is different from the rest of the paper, because the common perpendicular OY is not necessarily the solar meridian. Oy' is also different from the Oy axis of the l.o.s. reference frame, therefore we use a

different notation. In the $Ox'y'z$ reference frame the geometry is the same as in the equatorial case studied above, so that its final result may be applied

$$
\begin{aligned}
\mathrm{div}\,\boldsymbol{H} = {} & \frac{\Delta_{x'}H_{x'}^{(m)}}{\Delta x'} + \frac{\Delta_{y'}H_{y'}^{(m)}}{\Delta y'} + \frac{\Delta_z H_z^{(m)}}{\Delta z} \\
& + \tan\theta\frac{\Delta_z H_{x'}^{(m)}}{\Delta z} \, ,
\end{aligned}
\tag{A.14}
$$

where the Δ's are taken along each respective axis.

One has now to rotate this result into the l.o.s. reference frame represented in the right part of Fig. A.2. In this reference frame, the $\boldsymbol{i}_{x'}$ unit vector along Ox' has the following coordinates

$$\boldsymbol{i}_{x'}\begin{cases} \cos\varphi \\ \sin\varphi \\ 0 \end{cases} . \tag{A.15}$$

Accordingly,

$$H_{x'}^{(m)} = H_x^{(m)}\cos\varphi + H_y^{(m)}\sin\varphi \, . \tag{A.16}$$

One has by rotational invariance

$$\frac{\Delta_{x'}H_{x'}^{(m)}}{\Delta x'} + \frac{\Delta_{y'}H_{y'}^{(m)}}{\Delta y'} = \frac{\Delta_x H_x^{(m)}}{\Delta x} + \frac{\Delta_y H_y^{(m)}}{\Delta y} \, , \tag{A.17}$$

so that finally

$$
\begin{aligned}
\mathrm{div}\,\boldsymbol{H} = {} & \frac{\Delta_x H_x^{(m)}}{\Delta x} + \frac{\Delta_y H_y^{(m)}}{\Delta y} + \frac{\Delta_z H_z^{(m)}}{\Delta z} + \frac{1}{\cos\theta} \\
& \times \left[\frac{\Delta_z H_x^{(m)}}{\Delta z}\sin\theta\cos\varphi + \frac{\Delta_z H_y^{(m)}}{\Delta z}\sin\theta\sin\varphi\right] .
\end{aligned}
\tag{A.18}
$$

The $\boldsymbol{R}$ vector coordinates can also be expressed as

$$\boldsymbol{R}\begin{cases} \sin\theta\cos\varphi \\ \sin\theta\sin\varphi \\ \cos\theta \end{cases} . \tag{A.19}$$

Accordingly, the above Eq. (A.18) simply results in Eq. (10) of the paper. The second line accounts for the line formation plane inclination with respect to the line-of-sight

Appendix A.1.3: General case

Let's introduce the l.o.s. basic unit vectors $\boldsymbol{i}$, $\boldsymbol{k}$ and $\boldsymbol{\ell}$ (l.o.s. vector), and let's consider their projections $\boldsymbol{i}_p$ and $\boldsymbol{k}_p$ along Oz onto the line formation plane perpendicular to the solar radius unit vector $\boldsymbol{R}$ (see Fig. A.3). $\boldsymbol{i}_p$ and $\boldsymbol{k}_p$ are not unit vectors and have to be evaluated as follows. Let's denote by A the extremity of the $\boldsymbol{i}$ vector, and by A' the extremity of the $\boldsymbol{i}_p$ vector. A' is the projection of A along Oz. The AA' line of Fig. A.3 is defined by the intersection of the two planes of equations $x = 1$ and $y = 0$, respectively. A' is the intersection of the AA' line with the line formation plane perpendicular to R whose equation is given above in Eq. (A.1). The coordinates of $\boldsymbol{i}_p$ are then

$$\boldsymbol{i}_p\begin{cases} 1 \\ 0 \\ -\dfrac{R_x}{R_z} \end{cases} . \tag{A.20}$$

Analogously for the $\boldsymbol{k}$ and $\boldsymbol{k}_p$ vectors, the BB' line of Fig. A.3 is defined by the intersection of the two planes of equations $x = 0$
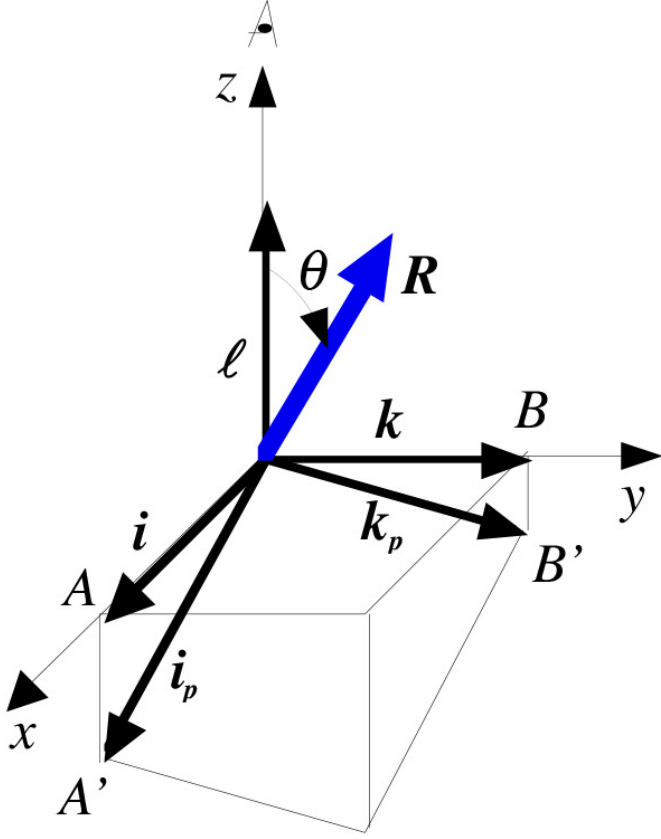
Fig. A.3. Projection of the unit vectors of the line-of-sight reference frame onto the line formation plane, which is perpendicular to the solar radius unit vector $\boldsymbol{R}$.

and $y = 1$ respectively and the coordinates of $\boldsymbol{k}_p$ are obtained by intersection with the line formation plane given in Eq. (A.1)

$$
\boldsymbol{k}_p \begin{cases} 0 \\ 1 \\ -\dfrac{R_y}{R_z} \end{cases} . \tag{A.21}
$$

We now apply the Ostrogradski's theorem. The elementary volume is obtained by projecting the elementary surface $\Delta x \Delta y$ along Oz onto the map plane, and by giving it a Δz thickness along Oz. As visible in Fig. A.3, the surface of the projected $\Delta x \Delta y$ is $\boldsymbol{i}_p \, \Delta x \times \boldsymbol{k}_p \, \Delta y$, which has for value $\Delta x \Delta y / R_z = \Delta x \Delta y / \cos \theta$, where θ is the heliocentric angle. The surfaces of the other sides of the elementary volume are respectively $\Delta x \Delta z$ and $\Delta y \Delta z$ (they are obtained by taking the product of $\boldsymbol{i}_p$ or $\boldsymbol{k}_p$ with $\boldsymbol{\ell}$, which is the unit vector along the l.o.s.). The divergence is then obtained as

$$
\begin{aligned}
\operatorname{div} \boldsymbol{H} \, \Delta x \Delta y \Delta z \;=\; & \left[\boldsymbol{H}^{(m)}(z + \Delta z) - \boldsymbol{H}^{(m)}(z) \right] \\
& \cdot \left[\boldsymbol{i}_p \, \Delta x \times \boldsymbol{k}_p \, \Delta y \right] \\
& + \left[\boldsymbol{H}^{(m)}(x + \Delta x) - \boldsymbol{H}^{(m)}(x) \right] \\
& \cdot \left[\boldsymbol{k}_p \, \Delta y \times \boldsymbol{\ell} \, \Delta z \right] \\
& + \left[\boldsymbol{H}^{(m)}(y + \Delta y) - \boldsymbol{H}^{(m)}(y) \right] \\
& \cdot \left[\boldsymbol{\ell} \, \Delta z \times \boldsymbol{i}_p \, \Delta x \right]
\end{aligned} \tag{A.22}
$$

leading to the expression given in Eq. (10). For clarity, the repeated and unchanged indices have been omitted in $\boldsymbol{H}^{(m)}$.
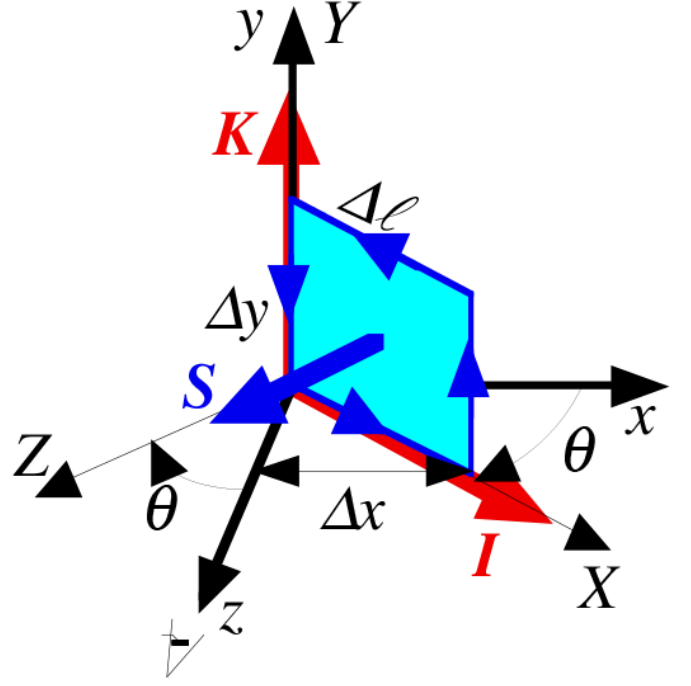
Fig. A.4. Elementary surface for the calculation of J_Z by applying the Stokes theorem to the circulation of the magnetic field vector along the oriented frontier of the surface. This figure is another view of Fig. A.1. Accordingly, the heliocentric θ angle is oriented by the Oy axis and is negative in the figure. The unit S vector is indeed the same as the unit R vector along the local solar radius.

Appendix A.2: Calculation of the curl

The curl is similarly obtained by applying the Stokes' theorem, which is that the flux of the curl through an elementary surface equals the "circulation" or work of the vector under study along the frontier of the surface, which is oriented as the surface itself. The elementary surfaces are the different faces of the elementary volume introduced above for the divergence. Analogously to the divergence derivation, we present first below a detailed calculation in the particular case of solar equator (Sect. A.2.1) and then the general case (Sect. A.2.2).

Appendix A.2.1: Case of a region located at solar equator

We consider the calculation of J_Z from the circulation of $\boldsymbol{H}$ along the oriented frontier of the elementary surface perpendicular to OZ. We have represented this elementary surface in Fig. A.4, which is another view of Fig. A.1. The circulation of $\boldsymbol{H}$ about the oriented surface is given by the scalar products

$$
\begin{aligned}
& \left[\boldsymbol{H}^{(m)}(y) - \boldsymbol{H}^{(m)}(y + \Delta y) \right] \cdot \boldsymbol{I} \Delta \ell \\
& + \left[\boldsymbol{H}^{(m)}(x + \Delta x) - \boldsymbol{H}^{(m)}(x) \right] \cdot \boldsymbol{K} \Delta y .
\end{aligned} \tag{A.23}
$$

For clarity, the repeated and unchanged indices have been omitted in $\boldsymbol{H}^{(m)}$. The unit vector $\boldsymbol{I}$ along OX has the following coordinates in the l.o.s. reference frame $Oxyz$

$$
\boldsymbol{I} \begin{cases} \cos \theta \\ 0 \\ -\sin \theta \end{cases} , \tag{A.24}
$$

whereas $\boldsymbol{K}$ is

$$\boldsymbol{K}\begin{cases} 0 \\ 1 \\ 0 \end{cases}. \tag{A.25}$$

As a consequence, the circulation of $\boldsymbol{H}$ is

$$\begin{aligned} &\left[H_x^{(m)}(y)\cos\theta - H_z^{(m)}(y)\sin\theta\right]\Delta\ell \\ &+\left[H_y^{(m)}(x+\Delta x)\right]\Delta y \\ &-\left[H_x^{(m)}(y+\Delta y)\cos\theta - H_z^{(m)}(y+\Delta y)\sin\theta\right]\Delta\ell \\ &-\left[H_y^{(m)}(x)\right]\Delta y\,. \end{aligned} \tag{A.26}$$

This circulation equals the flux of $\boldsymbol{J}$ through the surface, which is J_Z times the surface value, which is $\Delta\ell\Delta y = \Delta x\Delta y/\cos\theta$ following Eq. (A.9). This can be written as

$$\begin{aligned} J_Z \;=\;& \cos\theta\left[\frac{\Delta_x H_y^{(m)}}{\Delta x} - \frac{\Delta_y H_x^{(m)}}{\Delta y}\right] \\ &+\sin\theta\frac{\Delta_y H_x^{(m)}}{\Delta y}\,, \end{aligned} \tag{A.27}$$

which is Eq. (15) of the paper in the case of the surface located at equator, where the coordinates of the $\boldsymbol{R}$ vector are given by Eq. (A.19) with $\varphi = 0$.

Appendix A.2.2: General case

Referring now to Fig. A.3, the sides of the elementary volume are respectively $\boldsymbol{i}_p\Delta x$, $\boldsymbol{k}_p\Delta y$ and $\boldsymbol{\ell}\,\Delta z$. The circulation of $\boldsymbol{H}$ is given by its scalar product with each of these elementary vectors, eventually reversed following the surface orientation. This leads to

$$\begin{aligned} J_Z\,\frac{\Delta x\Delta y}{R_z} \;=\;& \boldsymbol{J}\cdot\left[\boldsymbol{i}_p\,\Delta x\times\boldsymbol{k}_p\,\Delta y\right] \tag{A.28}\\ \;=\;& \left[\boldsymbol{H}^{(m)}(y) - \boldsymbol{H}^{(m)}(y+\Delta y)\right]\cdot\boldsymbol{i}_p\,\Delta x \\ &+\left[\boldsymbol{H}^{(m)}(x+\Delta x) - \boldsymbol{H}^{(m)}(x)\right]\cdot\boldsymbol{k}_p\,\Delta y \end{aligned}$$

which results in the expression given in Eq. (15). The flux through the two other faces, which are respectively perpendicular to the Ox and Oy of the line-of-sight reference frame, gives the current components along those axes

$$\begin{aligned} J_y\,\Delta x\Delta z \;=\;& \boldsymbol{J}\cdot\left[\boldsymbol{\ell}\,dz\times\boldsymbol{i}_p\,\Delta x\right] \tag{A.29}\\ \;=\;& \left[\boldsymbol{H}^{(m)}(z+\Delta z) - \boldsymbol{H}^{(m)}(z)\right]\cdot\boldsymbol{i}_p\,\Delta x \\ &+\left[\boldsymbol{H}^{(m)}(x) - \boldsymbol{H}^{(m)}(x+\Delta x)\right]\cdot\boldsymbol{\ell}\,\Delta z \end{aligned}$$

and

$$\begin{aligned} J_x\,\Delta y\Delta z \;=\;& \boldsymbol{J}\cdot\left[\boldsymbol{k}_p\,\Delta y\times\boldsymbol{\ell}\,\Delta z\right] \tag{A.30}\\ \;=\;& \left[\boldsymbol{H}^{(m)}(z) - \boldsymbol{H}^{(m)}(z+\Delta z)\right]\cdot\boldsymbol{k}_p\,\Delta y \\ &+\left[\boldsymbol{H}^{(m)}(y+\Delta y) - \boldsymbol{H}^{(m)}(y)\right]\cdot\boldsymbol{\ell}\,\Delta z\,. \end{aligned}$$

This results in the expressions given in Eqs. (16-17). Again, for clarity, the repeated and unchanged indices have been omitted in $\boldsymbol{H}^{(m)}$.

These three derived current density vector coordinates are not all taken in the same reference frame. The frame rotation is fully accounted for in Sect. 3.3, in which all the coordinates of the current density vector are finally derived in both reference frames.